

1 Computational Model to Unravel the Function of Amyloid- β 2 Peptides in Contact with a Phospholipid Membrane

3 Dinh Quoc Huy Pham, Pawel Krupa, Hoang Linh Nguyen, Giovanni La Penna,* and Mai Suan Li*



Cite This: <https://dx.doi.org/10.1021/acs.jpcb.0c00771>



Read Online

ACCESS |



Metrics & More

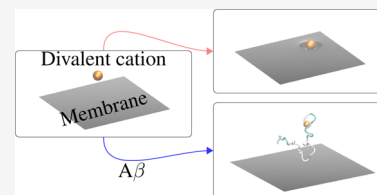


Article Recommendations



Supporting Information

4 **ABSTRACT:** Divalent cations have a strong impact on the properties of phospholipid
5 membranes, where amyloid- β peptides exert effects related to possible functional or
6 pathological roles. In this work, we use an atomistic computational model of dimyristoyl-
7 phosphatidylcholine (DMPC) membrane bilayers. We perturb this model with a simple
8 model of divalent cations (Mg^{2+}) and with a single amyloid- β ($A\beta$) peptide of 42 residues,
9 both with and without a single Cu^{2+} ion bound to the N-terminus. In agreement with the
10 experimental results reported in the literature, the model confirms that divalent cations locally
11 destabilize the DMPC membrane bilayer and, for the first time, that the monomeric form of
12 $A\beta$ helps in avoiding the interactions between divalent cations and DMPC, preventing significant effects on the DMPC bilayer
13 properties. These results are discussed in the frame of a protective role of the diluted $A\beta$ peptide floating around phospholipid
14 membranes.



15 ■ INTRODUCTION

16 Alzheimer's disease is a degenerative disease, with one
17 histological hallmark being extracellular deposits in the central
18 nervous system.¹ These deposits are made of amyloid peptides
19 originated by the amyloid precursor protein (APP), a trans-
20 membrane protein with a multimodal function.² Amyloid- β
21 ($A\beta$) peptides are produced with proteolysis of APP at the
22 membrane interface, by the enzymes β and γ -secretases. The γ
23 cleavage, which produces most of the neurotoxic peptides
24 (39–42 residues), occurs deeper in the membrane bilayer
25 compared to the β cleavage.³ The production of these toxic
26 peptides at the membrane interface can have many important
27 implications,⁴ even before peptide aggregation could occur and
28 when oligomers are more abundant than protofibrils:^{5,6} (i) the
29 toxic pathway can be influenced by interactions between
30 peptides and of peptides with the membrane; (ii) the peptide,
31 depending on its concentration, can destabilize the membrane,
32 contributing to cell instability and neuron death (apoptosis).
33 Both these effects are eventually exerted in a complex frame,
34 with many molecules present: APP N-terminus (before the
35 cleavage); peptides in monomeric, oligomeric, and prefibrillar
36 assemblies; other cofactors like metal ions. Thus, even at the
37 monomer level, the interactions between amyloid peptides and
38 biological membranes are still poorly understood.⁷ More
39 complete models are required to contribute to recent views of
40 APP and $A\beta$, where $A\beta$ aggregation is interpreted as a loss of
41 functional $A\beta$ monomers.⁸

42 Molecular simulations, particularly molecular dynamics
43 (MD), became a standard tool of computational biology to
44 study molecular interactions in such complex frames.⁹ Despite
45 the large number of simulation studies involving $A\beta$
46 monomers,^{10,11} oligomers,^{12,13} and fibril-like assemblies,^{14–18}
47 with all species in contact with membrane models, the role of

48 cofactors abundant in the environment of neurons have seldom
49 been taken into account.¹⁹ Among these cofactors, divalent
50 ions, and especially copper, are relevant for a correct
51 physiology of the synapse.²⁰ Some of the known facts are
52 summarized below.

1. Copper (Cu) and zinc (Zn) are particularly abundant in
the synaptic region. While physiological Cu(II) concen-
tration released within the synaptic cleft during synaptic
vesicle release is 15 μM , it achieves 300 μM
concentration upon neuronal depolarization.^{21,22} The
hypothesis of copper buffering activity of membrane
proteins was proposed for prion (see ref 22 and
references therein) and APP (ref 23 and references
therein). These concentrations are many orders of
magnitude larger than that inside the cell, where Cu, for
instance, is present in negligible amount as an ion
available to interactions.^{24,25} The addressing of APP as a
copper mediator has been discovered²⁶ and lately
associated to many neurodegenerative disorders.^{20,27,28}
2. Divalent cations change membrane structure, transport
properties,^{29–31} and reactivity,³² thus possibly promot-
ing protein aggregates resembling ion channels and
membrane pores.^{33,34}
3. Cu ions in contact with $A\beta$ peptides form catalysts for
the production of reactive oxygen species, activating

Received: January 28, 2020

Revised: March 19, 2020

Published: March 26, 2020

Table 1. Summary of Simulations Analyzed in This Work^a

simulation	composition	number of replicas/trajectories	equilibration time (ns)	analysis time (ns)
DMPC CMD	2 × 77 DMPC H ₂ O + 37 K + 37 Cl + 13,511 H ₂ O	4	200	200
Mg/DMPC CMD	2 × 77 DMPC + Mg + 35 K + 37 Cl + 13,510 H ₂ O	3	200	200
Aβ/DMPC REMD	Aβ + 2 × 77 DMPC + 39K + 36 Cl + 13,511 H ₂ O	56	200	200
Cu–Aβ/DMPC REMD	Cu–Aβ + 2 × 77 DMPC + 38 K + 36 Cl + 13,511 H ₂ O	56	200	200
Aβ/DMPC CMD	Aβ + 2 × 77 DMPC + 39K + 36 Cl + 13,511 H ₂ O	10	500	500
Cu–Aβ/DMPC CMD	Cu–Aβ + 2 × 77 DMPC + 38 K + 36 Cl + 13,511 H ₂ O	10	500	500

^aAbbreviations: CMD—conventional MD; REMD—replica exchange MD; DMPC—dimyristoyl-phosphatidylcholine; Aβ—Aβ(1–42) peptide, charge –3; Cu–Aβ—Cu–Aβ(1–42) complex, charge –2. Reported times are per each replica. See the [Methods](#) section for details.

73 dioxygen molecules,^{35,36} and promoting oxidative
74 pathways.^{37–40}

75 Because of these important issues, the modeling of
76 interactions of divalent cations with lipid charged and
77 zwitterionic membranes is becoming a challenge.^{41–43} Indeed,
78 recent polarizable models explain the experimentally observed
79 strong interactions between Ca²⁺ and phosphate groups in
80 POPC bilayers.⁴³

81 In this work, we compare, for the first time, models of free
82 and peptide-bound divalent cations in interaction with
83 dimyristoyl-phosphatidylcholine (DMPC) bilayers, with spe-
84 cial emphasis on oxidized copper. Polarizable models of
85 interactions between divalent cations and biological macro-
86 molecules are still experimental.⁴³ Even for nucleic acids, the
87 contribution of Mg²⁺ to the stability of tertiary RNA folding is
88 intricate.⁴⁴ Overall, it is not trivial starting from an unbound
89 condition to sample bound conditions that are observed
90 experimentally. Copper binding is known to be fluxional and
91 strongly dependent on the environment.^{45,46} Therefore, we
92 separately applied two modeling techniques: (i) a naive
93 nonbonded model of Mg²⁺ that has been used to model the
94 free energy change for the exchange reaction between the
95 water solution and a protein,⁴⁷ and for neutralizing RNA
96 phosphate groups;⁴⁸ (ii) a bonded model of Cu²⁺ that has been
97 applied to describe a well-documented binding site for Cu–
98 Aβ(1–42) observed in experiments^{49–51} and extensively
99 modeled by MD simulations.^{56,52}

100 The models describe interactions between, respectively,
101 Mg²⁺ aqua-ions, Aβ(1–42), and Cu(II)–Aβ(1–42) mono-
102 mers with DMPC bilayers, the latter being a well-studied
103 molecular model of the biological membrane. The simple
104 model used for the Mg divalent aqua-ion^{47,48} can depict a first
105 approximation of the effects of Cu²⁺ ions that have the size
106 similar to Mg²⁺ when not bound to proteins. These effects
107 mimic those of oxidized Cu on the membrane structure when
108 Cu is released around a phospholipid membrane.

109 The model, investigated by means of multiple conventional
110 MD simulations (CMD, hereafter) and replica exchange MD
111 (REMD), is limited to Aβ monomers and to exogenous
112 addition of Aβ to the lipid membrane rather than to peptide
113 incorporation into the membrane during its assembly (see the
114 [Methods](#) section). This assumption is representative of the
115 functional conditions of Aβ close to a phospholipid membrane.
116 Also, *in vitro* experiments about Aβ–DMPC interactions
117 mediated by divalent cations have been performed mimicking
118 exogenous addition.^{53,54}

119 Finally, the role of divalent cations in cell signaling is more
120 general than in synapse.⁵⁵ Therefore, it is of utmost importance
121 to understand interactions of divalent cations with the neuron
122 membrane in the presence of modulating ions' ligands.

METHODS

123

A summary of the simulations performed in this work is
reported in [Table 1](#).

Setup of MD Simulations. The amyloid-β peptide of 42
residues [Aβ(1–42)], with and without a single bound copper
ion in the +2 oxidation state (Cu²⁺), was simulated with
constant temperature CMD and with REMD methods, in
order to sample the configurational space under *in vitro* studies
and physiologically relevant temperatures of, respectively, 303
and 311 K (30 and 38 °C, respectively). The peptide and the
ions were put in contact with a bilayer composed of 1,2-
dimyristoyl-*sn*-glycero-3-phosphocholine (abbreviated as
DMPC hereafter) lipid molecules.

The sequence of Aβ(1–42) is

136

DAEFRHDSGY₁₀ EVHHQKLVFF₂₀ AEDVGSCKGA₃₀

IIGLMVGGVV₄₀ IA

with amino acids indicated with the one-letter code. We used
the Amber16 package,⁵⁶ with the FF14SB⁵⁷ force-field for the
peptide and monovalent ions (KCl), the TIP3P water model⁵⁸
for the explicit water solvent, and LIPID14⁵⁹ for the DMPC
molecules. AMBER FF14SB force-field is an improved version
of FF99SB⁶⁰ used in our previous simulations.^{52,61} Older
CHARMM force-fields tend to provide better results for Aβ
peptide than old AMBER force-fields.^{62,63} Also, OPLS-AA has
been combined with Cu-binding and Aβ oligomers.^{64,65}
Nevertheless, recent force-fields, especially AMBER FF14SB
and CHARMM36m, provide good agreement with exper-
imental data for Aβ.^{66,67} Moreover, AMBER FF14SB is fully
consistent with LIPID14 force-field,⁵⁹ which is expected to
provide optimal accuracy for both lipids and peptide in the
simulations that include both species. In conclusion, the
AMBER FF14SB is a good compromise to describe peptide,
lipids, water, and divalent cations in a unified manner. The use
of more recent force-fields for intrinsically disordered proteins,
like Aβ peptides, will be pursued in the future, after a detailed
comparison between experiments and simulations in general-
ized ensembles will be reported in the context of amyloid
peptides.

We assumed the physiological (pH ≈ 7) protonation state
for amino acid side chains and free termini. Thus, the charge of
Aβ(1–42) is –3 (the N-terminus is protonated and the C-
terminus is deprotonated). The parameters for copper and
copper-bound amino acids were the same as those used in our
previous MD and REMD simulations.^{52,61} Cu is bound to N
and O of Asp 1, Nδ of His 6, and Ne of His 13, the latter
protonated at Nδ. His 14 is neutral and protonated in Ne, like
His 6.

167

Bond distances and angles involving Cu contribute to harmonic energy terms, with stretching constants, bending constants, and equilibrium values set as fitting parameters of quantum-mechanics calculations at the density-functional level of approximation for truncated models (see Methods shown in ref 52). All the dihedral angles, where Cu has index 2 or 3, do not contribute to the potential energy, while those with Cu with index 1 or 4 are obtained by the AMBER99SB force-field where heavy atoms have the same dihedral indices of Cu. Point charges are derived from the restrained electrostatic potential method,^{68,69} where the electrostatic potential mapped onto the solvent-accessible surface was obtained at the density-functional level of truncated models (see ref 52 for details). Excess of net charge, obtained by merging point charges of truncated models into AMBER FF14SB amino acids, was distributed to C β and H β of Asp 1, His 6, and His 13 when these residues are bound to Cu²⁺. Lennard-Jones parameters for Cu are reported in the literature.⁷⁰ The Cu²⁺ coordination geometry in this empirical force-field is approximately square-planar, with the fifth axial coordination always available to electrostatic interactions, as shown in previous simulations performed with the same force-field.³⁶ The root-mean-square deviation (rmsd) between configurations obtained with this empirical force-field and minimal-energy configurations obtained including explicit electrons (like in density-functional theory applied to truncated models) is small.

As for the free divalent cation, we used the so-called “dummy” cation model for Mg²⁺.⁴⁷ This model has been used together with AMBER99SB phosphate groups,⁴⁸ where it showed reasonable electrostatic properties. Even though this model is a very crude approximation of divalent cations, it is far more reliable than a single site with point charge +2. A comparison between the affinity of divalent and monovalent cations for the DMPC membrane has been performed by umbrella sampling estimates of free energy differences (see the Supporting Information).

An initial lattice model of the DMPC bilayer was built, using 77 DMPC molecules per layer, with an approximate area per molecule of 62 Å². An orthorhombic simulation cell was built, with the cell side along zeta, the latter direction normal to the DMPC layer, initially set to 70 Å. The space between the periodic images of the bilayer was filled with 13,511 water molecules, initially at the density of 1 g/cm³, according to the TIP3P model of bulk water at room conditions. KCl was added in the same space, according to an approximate bulk concentration of 0.1 M. Ions were added randomly replacing water molecules in the initial configuration. The number of Cl⁻ anions was adapted to the change of net charge because of addition of the peptide (see below). The net charge of the simulation cell was always zero.

Initial configurations of amyloid- β monomer, without copper (charge -3) and with copper (charge -2, because of N-terminus deprotonation), were inserted in the space filled by the water molecules. The same was done for the single divalent cation. The space occupied by water on each side of the bilayer is, initially, 70 Å along the *x* and *y* direction, and 140–34 Å along the *z* direction, being the initial thickness of the bilayer approximately 34 Å. The bulk concentration of the divalent cation in this cell is, therefore, 3.2 mM, thus being in the range of the bulk concentration used for Ca, Mg, Zn, and Cu *in vitro* experiments. With a few exceptions, *in vitro* experiments use concentrations, both of peptide and divalent ions, about 2 orders of magnitude larger than *in vivo* in the synaptic cleft of

CNS neurons (in the order of ~10 μ M, physiologically, and 100 μ M upon neuronal depolarization, see the Introduction section).

To remove eventual atomic overlaps produced by each initial configuration setup, we performed 25,000 steps of steepest decent energy minimization, followed by other 25,000 steps of conjugate gradient energy minimization.

The initial coordinates for the CMD and REMD simulations are included as the Supporting Information in the protein data bank (PDB) file format (the first configuration) and as the compressed (Bzip2) XYZ format.

MD Simulation Protocol. We simulated CMD trajectories in the isobaric-isothermal (*NPT*) statistical ensemble, at the constant temperature *T* of 303 and 311 K and at the pressure *P* of 1 atm. Temperature was controlled by a Langevin thermostat⁷¹ with a collision frequency of 2 ps⁻¹. Pressure was controlled by a stochastic barostat, with a relaxation time of 100 fs. The SHAKE algorithm⁷² was applied to constrain bonds involving hydrogen atoms. A cut-off of 10 Å was applied for nonbonded interactions and the particle mesh Ewald algorithm⁷³ was used to compute long-range Coulomb and van der Waals interactions. The simulation time-step was 2 fs.

In order to increase the sampling, we collected several trajectories for each system, starting from different initial conditions. As for DMPC and Cu/DMPC systems, only initial velocities were changed, while for the other systems, the positions of ions and peptide atoms were also changed. The composition of each system and some parameters related to sampling is reported in Table 1.

Replica-Exchange MD Simulation. The REMD simulation was carried out with 56 replicas (or trajectories) corresponding to 56 temperatures ranging from 273 to 500 K. The configuration with minimal energy was distributed among 56 replicas, and each replica was equilibrated in 200,000 steps at the temperature chosen in the temperature distribution. After equilibration, the REMD simulation started, for a total time, for each replica, of 400 ns. The exchange of temperature between pair of replicas was attempted every 500 steps of simulation. The REMD simulation is used here mainly to capture the statistical contribution of extended peptide configurations and partially disordered layers, configurations that are rarely sampled at temperatures in the range where the force-field is accurate. The acceptance rate of REMD simulations was, on average, 20 and 21% for, respectively, A β (1–42) and Cu–A β (1–42).

The behavior of lipid order parameters as a function of temperature (data not shown here) shows that the DMPC bilayer is, at the temperature closest to that of the human body (37 °C, 310 K), in the liquid crystalline phase. The configuration sampling the temperature of 311 K are, therefore, analyzed in detail in the following.

To avoid possible bias due to the choice of initial configurations, we used the second half (500 ns) of each simulation for analysis (see Table 1). In REMD, we used equilibration and sampling times (200 ns) shorter than those used in CMD because of the faster convergence of REMD compared to CMD. The choice of these sampling times is dictated by the time evolution of structural properties. See for instance rmsd in the Supporting Information and the distance along the *z* axis between the bilayer center and the closest atom of the peptide (see Figure 5 and comments in the “Results” section).

293 **Analysis. Structural Properties.** rmsd and radius of
 294 gyration (R_g) were calculated for all $A\beta(1-42)$ atoms using
 295 the initial $A\beta(1-42)$ structure as a reference for the rmsd
 296 measurement. The secondary structure of $A\beta(1-42)$ was
 297 analyzed using DSSP software included in the cpptraj tool,⁵⁶ a
 298 part of AmberTools package. Three regular types of the
 299 secondary structure were distinguished in the analysis: helices
 300 (α , 3–10, and π), β -sheets (parallel and antiparallel), and
 301 turns, while the residues in other conformations were treated
 302 as unstructured (coil). The solvent-accessible surface area was
 303 calculated for $A\beta(1-42)$ and lipids using linear combinations
 304 of terms composed from the pairwise overlaps method,⁷⁴
 305 implemented in cpptraj.

306 The radial distribution function (RDF) measures the
 307 probability to have the distance between two sites within a
 308 given distance range, $N(r)$. As usual for liquids and polymers,
 309 this quantity is then divided for the same probability for the
 310 ideal gas with the same uniform density of sites, $N_{id}(r)$: $g(r) =$
 311 $N(r)/N_{id}(r)$. The function $g(r)$ approaches the limit $g(r) = 1$
 312 when $r \rightarrow \infty$, that is, when the two sites in the pair become not
 313 correlated.

314 The bilayer thickness is defined as the distance between the
 315 two planes formed by phosphor atoms belonging to each layer.
 316 The roughness of a layer is defined as the standard deviation of
 317 z coordinates of phosphor atoms within each layer.

318 The number of contacts is defined as the count of the usual
 319 distance-based step-like variable

$$\begin{aligned} \text{CN}_2 &= \sum_{i,j} S_{i,j} \\ S_{i,j} &= 1 \text{ if } r_{i,j} \leq 0 \\ S_{i,j} &= 0 \text{ if } r_{i,j} > 0 \\ r_{i,j} &= |\mathbf{r}_i - \mathbf{r}_j| - d_0 \end{aligned} \quad (1)$$

321 with i and j running over different sets of atom pairs, each term
 322 of the pair contained in a different portion of the system. When
 323 the two sets of atoms identify, respectively, atoms belonging to
 324 positively charged groups ($N\zeta$ in Lys and $N\eta$ in Arg) and
 325 negatively charged groups ($C\gamma$ in Asp and $C\delta$ in Glu), we
 326 address the contact as an intramolecular salt bridge (SB). The
 327 number of such contacts is indicated as SB, and the d_0
 328 parameter is chosen as 4 Å. As for generic inter-residue
 329 contacts, we measured the distance between the centers of
 330 mass of side chains in the two involved residues. In this case, d_0
 331 is chosen as 6.5 Å. When the contact between amino acids and
 332 lipid molecules is addressed, the center of mass of DMPC
 333 molecules is used, and the d_0 distance is 4.5 Å.

334 The $S(\text{CH})$ order parameter is the average of the second-
 335 rank projection of the chosen C–H bond over the axis of
 336 preferred orientation of lipid molecules

$$S = \frac{1}{2} \langle 3 \cos^2 \theta - 1 \rangle \quad (2)$$

337 where θ is the angle between the C–H bond and the z bilayer
 338 axis, as in the liquid crystal phase.

340 **Elastic Moduli.** Elastic moduli of the lipid bilayer were
 341 calculated by fitting suitable ensemble averages with the
 342 following equations⁷⁵

$$\begin{aligned} \langle |\hat{n}_q^\parallel|^2 \rangle &= \frac{k_B T}{K_c q^2} \\ \langle |\hat{n}_q^\perp|^2 \rangle &= \frac{k_B T}{K_\Theta + K_{tw} q^2} \end{aligned} \quad (3)$$

where K_c , K_Θ , K_{tw} are bending, tilt, and twist elastic moduli,
 respectively, k_B is Boltzmann constant, T is temperature, and \hat{n}_q
 is the reciprocal space vector determined as summarized below
 (see also the Supporting Information of refs 75 and 76).

The xy plane of the membrane is discretized to a square 8×8
 grid. The orientation vector of lipid molecule j is $\mathbf{n}_j^{(\alpha)}(x, y, z)$
 with α 1 or 2 for upper and lower layers, respectively. Each
 vector points from the midpoint between P and C2(glycerol)
 atoms to the midpoint between the terminal C atoms of the
 lipid tails. The orientation vectors are projected onto the xy
 plane and are mapped onto the 8×8 grid, providing $n^{(\alpha)}(x, y)$.
 Fast Fourier transform is used to obtain $n_q^{(\alpha)}$, where q is the
 reciprocal space index. From $n_q^{(\alpha)}$ we obtain the quantity

$$\hat{n}_q = \frac{1}{2} [n_q^{(1)} - n_q^{(2)}] \quad (4)$$

that is decomposed into longitudinal (\hat{n}_q^\parallel) and transverse (\hat{n}_q^\perp)
 components

$$\begin{aligned} \hat{n}_q^\parallel &= \frac{1}{q} [\mathbf{q} \cdot \hat{n}_q] \\ \hat{n}_q^\perp &= \frac{1}{q} [\mathbf{q} \times \hat{n}_q] \cdot \hat{z} \end{aligned} \quad (5)$$

Finally eq 3 is used to average according to the collected
 sampling of lipid molecules.

RESULTS

Addition of a Divalent Cation to the DMPC Bilayer.

The affinity of Mg^{2+} for the DMPC bilayer was measured using
 the umbrella sampling method (see the Supporting Informa-
 tion, Figure S1). The free energy minimum was found at 17 Å
 from the bilayer center, thus corresponding to the average
 minimal distance between P atoms belonging to opposite
 layers (see below). The flatter shape of free energy around the
 minimum in the case of Na^+ is due to the equivalent
 interactions of Na with phosphate and carbonyl groups of
 DMPC. These interactions allow a deeper penetration of Na
 into the bilayer than Mg. The binding free energy of Mg^{2+} was
 estimated as about four times that of Na^+ and equal to
 approximately 2.0 and 0.5 kcal/mol, respectively. The range of
 negative values of the potential of mean force (PMF) is wide,
 indicating that the dragging of water molecules below the
 surface of the lipid membrane forms stable structures. This
 difference favors the binding of Mg to the DMPC surface
 compared to Na. This difference is opposite to what is
 expected on the basis of dehydration free energy that should
 favor Na compared to Mg, being the hydration free energy at
 300 K about five times more negative for Mg compared to
 Na.⁷⁷ This effect is due to the strong electrostatic interactions
 formed by Mg when absorbed by phosphate groups, together
 with a significant drift of water molecules toward the bilayer
 center along with the cation's penetration. Therefore, these
 interactions with phosphate oxygen and with residual water
 molecules strongly compensate the loss of water molecules
 from the Mg first-coordination sphere when Mg is driven from

392 the bulk water toward the bilayer center. The PMF plot
 393 (Figure S1) shows that there is a significant energy barrier
 394 hindering Na^+ and Mg^{2+} ions to enter middle of the lipid
 395 membrane, equal to approximately 6.5 and 7.5 kcal/mol,
 396 respectively. The obtained barrier is smaller than the one
 397 reported in other computational works, which is in the range of
 398 15–24 kcal/mol for Na^+ . This may be caused by the use of
 399 different lipid bilayer models, force-field parameters, and
 400 sampling.^{78–80} The cited works show presence of shallow
 401 minimum at distance of 14–18 Å from the bilayer center,
 402 indicating possible binding affinity, similar to our results.
 403 However, all these values, including experimental observations,
 404 are subjected to rather large errors because of the used
 405 methodologies and simplifications of models.⁸⁰

406 All of the three CMD trajectories of Mg/DMPC display a
 407 rapid approach of the divalent cation (Mg^{2+}) from the bulk to
 408 the initially closest layer. After 200 ns, the divalent cation is
 409 trapped by phosphate groups of DMPC. Because the three
 410 CMD trajectories are equivalent in several average properties
 411 (like the RDF g , see the Methods section), the average over the
 412 3 trajectories is analyzed in the following. We indicate the
 413 cation-bound layer as layer 1 (L1) and the layer not affected by
 414 the binding as layer 2 (L2). The difference between g
 415 calculated for L1 and L2 is displayed in Figure 1. The divalent

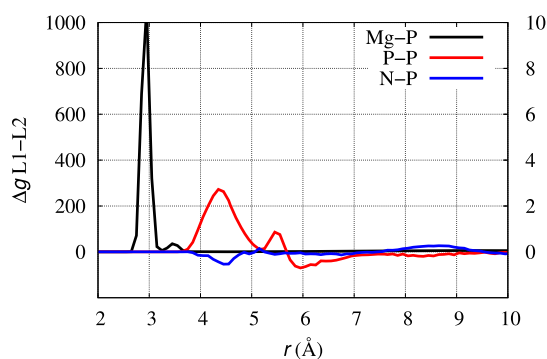


Figure 1. Difference between RDF (g) computed in Mg/DMPC for layer 1 (Mg-bound) and layer 2. Mg–P (black line); P–P (red line); N–P (blue line). Left y-axis is for the black line, and right y-axis is for red and blue lines.

416 cation (black) is bound to the phosphate oxygen atoms, thus
 417 displaying the coordination distance of 2.9 Å with respect to P
 418 atoms. Including the second-shell P atoms (the peak at 3.5 Å),
 419 the number of P atoms around the cation is 4. This
 420 coordination affects the average distance between charged
 421 groups within L1, as it is displayed by the P–P distances (red
 422 line), respectively, within each layer L1 and L2. In contrast,
 423 atoms farther than P from the perturbing cation are less
 424 affected, as shown by the difference in N–P distance
 425 distribution among the two layers (blue line).

426 The formation of a cluster of phosphate groups in L1
 427 induces the release of the electrostatic interactions within the
 428 head groups in each layer. Therefore, a consequence of
 429 phosphate neutralization by Mg binding to L1 is a change in
 430 the distribution of monovalent counterions at the interface of
 431 the two different layers. This effect is emphasized by plotting
 432 the difference in K–P RDF between the two layers and by
 433 comparing this quantity with the same quantity computed in
 434 the absence of the divalent cation (Figure S2 in the Supporting
 435 Information). In panel A, it can be noticed that the distribution

of K^+ in the presence of Mg (black curves) is more asymmetric 436
 than with no Mg (red curves). The low symmetry of K–P 437
 distribution in the absence of Mg (red curves) is due to 438
 sampling limitations. Indeed, the presence of Mg on the L1 439
 layer displays a “hole” in K distribution where there is a little 440
 excess in the absence of Mg. Because of the change in 441
 interactions between K^+ and P at short distance (the peaks at 442
 the left), there is also a decrease of bulk concentration within a 443
 distance of 1 nm from the P atoms. This change of the 444
 electrostatic properties between the two sides of the bilayer is 445
 equivalent to weak polarization of the membrane. This 446
 asymmetry is caused by the asymmetry in the P–P radial 447
 distribution (Figure S2B) that is due to the formation of the 448
 Mg–O(P) coordination. 449

The asymmetry of the interactions between divalent cations 450
 added from one side of the bilayer is consistent with the 451
 experimental data reported for exogenous addition of Cu^{2+} and 452
 Zn^{2+} to bilayer models (POPC/POPS mixtures).⁵³ The 453
 comparison between ^2H and ^{31}P ss-NMR spectra of POPC/ 454
 POPS molecules shows that P atoms are strongly affected, 455
 while the molecular tails in the hydrophobic region of the 456
 bilayer are almost unaffected. The addition of Cu^{2+} to these 457
 membranes induces the formation of smaller vesicles, thus 458
 showing a dramatic effect of this ion on the bilayer stability. 459

The effect of the divalent cation on the elastic property of 460
 DMPC is also significant. In Table 2, we report the elastic 461
 constants determined by the different simulations, with 462
 averages of eq 3 (see the Methods section) computed over 463
 all the acquired trajectories (see Table 1). 464

Table 2. Elastic Moduli of the DMPC Bilayer with No Addition (DMPC) and Interacting with, Respectively, a Divalent Cation (Mg/DMPC), the $\text{A}\beta$ Peptide ($\text{A}\beta$ /DMPC), and the Cu– $\text{A}\beta$ Peptide (Cu– $\text{A}\beta$ /DMPC)^a

elastic moduli	DMPC	Mg/DMPC	$\text{A}\beta$ /DMPC	Cu– $\text{A}\beta$ /DMPC
K_c (10^{-20} J)	7.859 (0.369)	14.568 (0.756)	13.316 (1.307)	15.210 (2.077)
K_θ (10^{-20} J/nm ²)	6.679 (0.191)	5.200 (0.200)	6.767 (0.241)	7.095 (0.200)
K_{tw} (10^{-20} J)	1.447 (0.010)	1.629 (0.006)	1.668 (0.061)	1.668 (0.042)

^aAverage is computed over 10 windows of 20 ns each, during the last 200 ns of each CMD trajectory. Standard error is within parenthesis.

The values are in the range of those found in DPPC 465
 atomistic simulations,⁷⁵ although the conditions (temperature, 466
 force-field, *etc.*) are different. The bending constant (K_c) of 467
 pure DMPC is smaller than that in all the other cases, where 468
 the DMPC is perturbed by exogenous addition of species. This 469
 change shows that the addition of any species on one side of 470
 the bilayer increases the rigidity of curvature because of the 471
 change exerted more on one layer than on the opposite layer. 472
 On top of this effect, that is due to the asymmetry of the 473
 addition, the tilt modulus (K_θ) is significantly smaller for Mg/ 474
 DMPC compared to the DMPC bilayer both unperturbed 475
 (DMPC) and with the peptide ($\text{A}\beta$ /DMPC and Cu– $\text{A}\beta$ / 476
 DMPC) floating over the bilayer surface. This additional 477
 information reveals that the formation of bridges between 478
 phosphate groups occurring in Mg/DMPC (see Figure 1) 479
 produces a cluster of 3–4 lipid molecules that changes the 480
 elasticity of DMPC. As described above (and also in detail 481
 below), the lipid molecules belonging to the cluster are more 482
 rigid and create a small hollow in the surface. Perturbation 483

484 exerted by Mg–phosphate interactions makes a little hollow
 485 over the bilayer surface affected by Mg binding. This little
 486 hollow can be observed looking at the configurations where
 487 Mg penetration is deep, like in Figure 2. This local
 488 perturbation allows the molecules neighbor to the cluster to
 489 more easily tilt with respect to the bilayer normal.

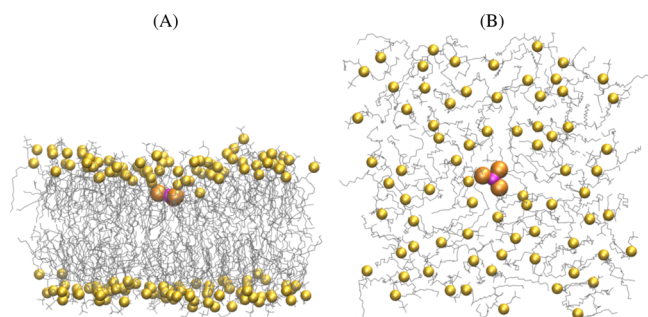


Figure 2. Configuration of Mg/DMPC where the distance between Mg (purple sphere) and the bilayer central plane is minimal along with the CMD simulations 1–3. P atoms in DMPC are represented as yellow spheres, and those within 3.5 Å from Mg are emphasized in orange. The other DMPC molecules are represented as thin bonds. Water and KCl are not displayed. Atomic radii are arbitrary. Panel (B) is the same structure in (A) observed from the *z* axis and with only lipid molecules in L1 displayed.

490 The effect of Mg addition to L1 does not significantly alter
 491 other structural parameters of the bilayer at the same
 492 temperature (see Table 3). For instance, the bilayer thickness

Table 3. Bilayer Structural Data Averaged over the Second Half of All Trajectories (avg.) and Selected Trajectories (traj./REMD)^a

simulation	area per lipid (Å ²)	thickness (Å)	roughness L1 (Å)	roughness L2 (Å)
DMPC	63.75(0.05)	34.4(0.2)	2.4(0.3)	2.5(0.4)
Mg/DMPC	63.75(0.05)	34.3(0.2)	2.5(0.4)	2.5(0.4)
Aβ/DMPC (REMD)	64.5(0.1)	34.4(0.2)	2.5(0.3)	2.5(0.3)
Cu–Aβ/DMPC (REMD)	64.4(0.1)	34.4(0.2)	2.5(0.3)	2.5(0.4)
Aβ/DMPC (avg.)	60.6(1.4)	35.6(0.6)	2.7(0.5)	2.7(0.5)
Cu–Aβ/DMPC (avg.)	60.6(1.2)	35.6(0.6)	2.7(0.5)	2.7(0.5)
Aβ/DMPC (traj. 1)	61.6(1.1)	35.5(0.5)	2.6(0.4)	2.6(0.4)
Aβ/DMPC (traj. 5)	60.8(1.6)	35.4(0.7)	2.7(0.4)	2.7(0.5)
Cu–Aβ/DMPC (traj. 8)	60.9(1.1)	35.6(0.5)	3.2(0.9)	3.3(0.9)

^aRoot-mean square errors are within brackets.

493 and area per lipid compare well with the values measured by
 494 diffraction studies for DMPC.⁸¹ Experiments report thickness
 495 at *T* = 303 and 323 K of, respectively, 36.7 and 35.2 Å², while
 496 in our MD simulation, at 311 K, the thickness is 34.4 Å². This
 497 small difference may be due to the slightly different way used
 498 to measure the thickness (see the Methods section and ref 81).
 499 The experimental area per lipid is 59.9 and 63.3 Å² at the same
 500 two probed temperatures of 63.8 at 311 K, respectively.
 501 Negligible effects are observed for the average roughness with
 502 the Mg²⁺ addition (see Table 3), thus confirming that any
 503 effect due to Mg/DMPC association is very localized in space.

We measured the order parameter, probed by means of 504
 S(CH) (see the Methods section), for C–H bonds in the 505
 methylene groups in the acyl chains of the lipid molecules. The 506
 profile of S(CH) along the chain does not change upon 507
 addition of the divalent cation (see Figure S5 and related 508
 discussion in the Supporting Information). This, again, shows 509
 that the perturbation made by the divalent cation is limited to 510
 the lipid head groups. 511

Exogenous Addition of the Aβ Peptide to the Bilayer. 512

In the REMD Aβ/DMPC and Cu–Aβ/DMPC simulations, 513
 the DMPC bilayer is in the liquid crystal phase at all the 514
 probed temperatures, consistently with similar MD simulations 515
 reported in the literature.⁸² The temperature dependence of 516
 the area per lipid in Aβ/DMPC REMD simulation is displayed 517
 in Figure 3, together with the available experimental results for 518

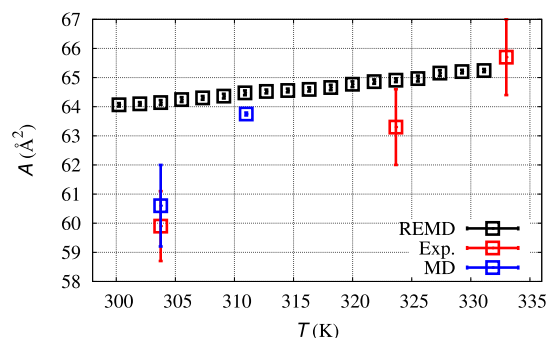


Figure 3. Area per lipid (*A*) as a function of temperature (*T*): average results for REMD simulation (black squares); experimental results at 303, 323, and 333 K (red squares⁸¹); average of 10 CMD simulations for Aβ/DMPC at 303 K and DMPC at 311 K (blue squares).

DMPC,⁸¹ the result for CMD at *T* = 311 K for DMPC, and the 519
 average of 10 CMD trajectories at *T* = 303 K described below. 520
 The behavior for Cu–Aβ/DMPC is not graphically distinct 521
 from Aβ/DMPC and, therefore, it is not displayed. The REMD 522
 simulation is able to capture the increase of area per lipid (*A*) 523
 as *T* increases as well as the area per lipid at high *T*, but it is 524
 dominated by high-*T* lipid configurations that are often 525
 exchanged in REMD with low-*T* configurations. However, 526
 REMD can adequately probe the possibility of peptide 527
 penetration at the highest area per lipid accessible, both by 528
 experiments and simulations, in the liquid crystal phase of 529
 DMPC. Therefore, it is expected that for lower *A*, peptide 530
 penetration would be more difficult than at high *T*. 531

In Figure S3 (see the Supporting Information), we display 532
 the RDF *g* for selected pairs to show the extent of penetration 533
 of N- and C-termini (respectively Nt and Ct) through the 534
 membrane surface (using P atoms in the pair) or toward the 535
 membrane center (using the terminal C atom in the two acyl 536
 chains of DMPC, Cf hereafter). The *g* function is measured at 537
T = 311 K, that is, the physiological temperature of biological 538
 membranes. The REMD trajectory at 311 K shows that the 539
 propensity for Aβ and Cu–Aβ N-termini to interact with the 540
 membrane surface is limited to the head groups of the DMPC 541
 bilayer, the P atoms. The peaks in Figure S3A (black lines for 542
 Aβ/DMPC) represent the electrostatic interaction between the 543
 positively charged Nt group of Aβ with the negatively charged 544
 phosphate groups (see also the number of SBs discussed 545
 below). The peptide N-terminus (residues 1–16) contains 546
 most of the charged side chains and it is the peptide segment 547
 involved in metal ion binding. For this reason, the behavior of 548

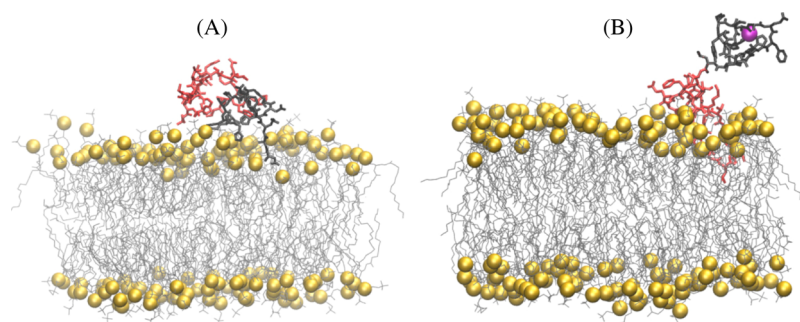


Figure 4. Configurations of $A\beta$ /DMPC (left) and $Cu-A\beta$ /DMPC (right) displaying the deepest penetration into the lipid bilayer in REMD simulations. The configurations are those where the distance between any peptide atom and any of the bilayer Cf atoms (the terminal methyl group of acyl DMPC side chains) is minimal along with the trajectory at $T = 311$ K. The peptide is represented as bonds (N-terminal residues 1–16 in black, C-terminal residues 17–42 in red), Cu as a purple sphere. P atoms in DMPC are represented as yellow spheres. The other DMPC molecules are represented as thin bonds. Water and KCl are not displayed. Atomic and bond radii are arbitrary.

549 N- and C-termini is expected to be different when they are
550 contact with a charged membrane. The approximate symmetry
551 of the g function measured for different layers in the bilayer
552 membrane (L1 and L2) shows that in both conditions, the N-
553 terminus of the peptide is floating above the membrane
554 surface, going back and forth from one layer to the other. The
555 lower symmetry of $A\beta$ /DMPC (black lines) compared to $Cu-$
556 $A\beta$ /DMPC (red lines) shows that even wide REMD sampling
557 is not fully adequate to capture the intrinsic symmetry of the
558 system when electrostatic interactions occur.

559 The $A\beta$ peptide Nt atom approaches the P atoms at 3.5 Å,
560 while Cu in $Cu-A\beta$ rarely reaches a distance lesser than 6.5 Å.
561 The Cu-binding to $A\beta$ reduces the interactions between the N-
562 terminal region of the $A\beta$ peptide and DMPC head groups,
563 producing a more symmetric g function among the two layers.
564 This effect is expected because the interaction with Cu spreads
565 the positive charge over the Cu-bound residues, while in the
566 charged N-terminus (when not bound to Cu) of the $A\beta$
567 peptide, the positive charge density is higher, and the
568 interactions with negatively charged groups at the bilayer
569 interface are more likely.

570 The peptide rarely penetrates the membrane bilayer, as
571 shown by the g function for pairs involving the Cf atoms (the
572 bottom of the acyl chains in lipid molecules, Figure S3C,D).
573 According to the bilayer structure (see the results reported
574 below), the average distance between P atoms and the center
575 of the bilayer is about 17 Å. Therefore, the Nt atom for $A\beta$ /
576 DMPC (black lines in panel C) and the Ct atom in $Cu-A\beta$ /
577 DMPC (red lines in panel D) significantly approach the bilayer
578 center, showing deep penetration in rare configurations in the
579 trajectory. Noticeably, when Cu is bound to the peptide (red
580 lines), penetration occurs from the C-terminus, while when Cu
581 is absent, the N-terminus is allowed to move from the surface
582 (P atoms) toward the bilayer center. The representation of this
583 change in penetration is better understood, examining the few
584 snapshots contributing to g at short distances in, respectively,
585 Cf–Nt ($A\beta$ /DMPC, Figure S3C) and Cf–Ct ($Cu-A\beta$ /
586 DMPC, Figure S3D). In Figure 4 we display, left and right
587 panels, one of such configurations for, respectively, each of the
588 two systems. It can be observed that a common feature of the
589 peptide structure in these configurations is the breaking of
590 cross-talk between the N- and C-termini. This cross-talk is
591 always present when the peptides (both $A\beta$ and $Cu-A\beta$) are in
592 water solution, and it is often maintained when the peptide
593 interacts with the membrane surface. The interplay between

the release of intrapeptide interactions and penetration into the
bilayer is discussed in more detail below.

The number of intramolecular SBs within the peptide
(Table 4) is consistent with the data reported for the

Table 4. Structural Data Averaged over the Second Half of All Trajectories (avg.) and Selected Trajectories (traj./REMD)^a

simulation	SASA (nm ²)	SB	β (%)	Helix (%)	R_g (nm)
$A\beta$ /DMPC (avg.)	33(3)	2.7(1.1)	7.9	11.1	1.1
$Cu-A\beta$ /DMPC (avg.)	35(2)	2.9(1.1)	6.2	11.2	1.1
$A\beta$ /DMPC (REMD)	35(3)	2.5(1.2)	9	12	1.1
$Cu-A\beta$ /DMPC (REMD)	38(3)	2.2(1.0)	8	7	1.3
$A\beta$ /DMPC (traj. 1)	39(2)	3.0(0.9)	0.0	15.1	1.3
$A\beta$ /DMPC (traj. 5)	30(1)	3.1(0.8)	2.8	1.9	1.0
$Cu-A\beta$ /DMPC (traj. 8)	33(2)	3.2(0.6)	0.1	20.0	1.0
$A\beta$	32(2)	2.8(1.0)	10.0	4.2	1.0
$Cu-A\beta$	36(2)	2.8(1.3)	0.6	1.2	1.1

^aSee the Methods section for definitions. Root-mean-square errors are within brackets.

simulation of the same peptides in water (last columns). For
 $A\beta$ /DMPC, SB is similar to the value in water, with N(Asp 1)
providing a contribution of approximately 1 in both cases. This
shows that despite the few interactions between the N
terminus and the phosphate groups of DMPC, the intra-
molecular SB involving N(Asp 1) in the peptide is not
statistically broken, and the monomeric peptide keeps the
network of intramolecular SBs almost intact. This result is
consistent with the rare events of membrane penetration
observed in REMD at $T = 311$ K. Also, in $Cu-A\beta$ /DMPC, SB
does not change with respect to the value in water. These data
show that the N-terminus of $A\beta(1-42)$ and $Cu-A\beta(1-42)$ is
bent toward the peptide by, respectively, intramolecular SBs
and covalent bonds involving Cu. Thus, N-terminus is rarely
released by the peptide cross-talk to form new interactions
with the DMPC phosphate groups.

The bilayer structure (Table 3) shows only moderate
propensity for larger thermal fluctuations, induced by the
perturbation due to weak interactions with the peptide, and a
small increase in thickness.

Because of the extended conformational sampling in REMD,
in both cases, the peptide N-terminus moves back and forth

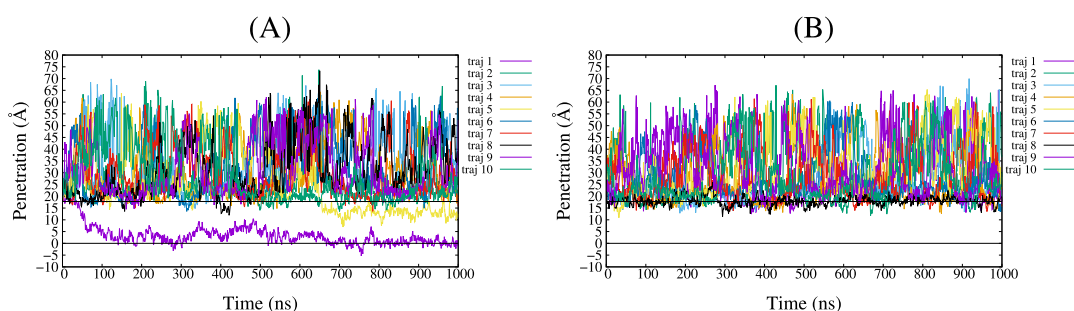


Figure 5. Penetration of $A\beta(1-42)$ (left, $A\beta$ /DMPC) and $Cu-A\beta(1-42)$ (right, $Cu-A\beta$ /DMPC) into the lipid bilayer. The y axis is the z coordinate of the lowest atom (minimal z) of the peptide. The horizontal line at $y = 0$ indicates the center of geometry of the bilayer which is the average of z coordinates of all DMPC's atoms. The horizontal line at 17.7 Å shows the average position of all P atoms.

620 between the two layers because of the usual periodic boundary
 621 conditions used in simulations. As a consequence of the weak
 622 interactions between the peptide and the DMPC bilayer, the
 623 distributions of K–P and P–P distances are approximately
 624 symmetric among the two layers and almost identical to those
 625 of pure DMPC (data not shown here). The peptide does not
 626 change the distribution of monovalent ions.

627 The $S(CH)$ -order parameter is not sensitive to the presence
 628 of the peptide, irrespective of the Cu-binding to the peptide.
 629 This, again, shows that the interactions of the peptide are
 630 limited to the lipid head groups and do not affect the
 631 hydrophobic core of the lipid bilayer.

632 In order to extract more information about possible specific
 633 interactions favoring asymmetry in structural and electrostatic
 634 properties among the two layers, in the following, we compare
 635 10 separated long (1 μ s) CMD simulations performed for both
 636 the $A\beta$ /DMPC and $Cu-A\beta$ /DMPC models.

637 **Comparing Different Peptide/DMPC Associations.** In
 638 this section, the NPT -ensemble MD simulations (that we
 639 indicate as CMD) of $A\beta$ /DMPC and $Cu-A\beta$ /DMPC are
 640 described. Because the sampling in CMD is more limited than
 641 in REMD, the different trajectories allow a comparison
 642 between different kinds of $A\beta$ /DMPC and $Cu-A\beta$ /DMPC
 643 association.

644 In Figure 5, in order to describe the type of association, the
 645 distance along the z axis between the bilayer center and the
 646 closest atom of the peptide is displayed as a function of time
 647 for all trajectories. Among 10 1 μ s-long trajectories acquired
 648 for each of the two species, $A\beta$ /DMPC (panel A) and $Cu-$
 649 $A\beta$ /DMPC (panel B), respectively, we observe the rapid
 650 incorporation of the peptide into the bilayer in one trajectory
 651 only, trajectory 1 of $A\beta$ /DMPC. As for $A\beta$ /DMPC, we observe
 652 partial incorporation after 600 ns for trajectory 5, while for
 653 $Cu-A\beta$ /DMPC, moderate bilayer penetration is observed for
 654 trajectory 8. These data show that in most of the cases, the
 655 peptide interacts with head groups (around P atoms). On
 656 average, the distance between Cu and the center of the
 657 membrane is 42.0 ± 10.6 Å for $Cu-A\beta$ /DMPC compared to
 658 15.3 ± 2.4 Å for Mg in Mg/DMPC. In all simulations, the
 659 bilayer thickness is about 34 Å (see Table 3 and discussion
 660 below); thus, the average distance between P atoms and the
 661 central plane of the bilayers is never below 17 Å. The approach
 662 of Mg towards the bilayer central plane does not significantly
 663 drift, on average, the P atoms towards the center of the bilayer,
 664 because the density of P atoms projected along the z axis does
 665 not change (data not shown here). However, as described
 666 above, the perturbation makes a little hollow over the bilayer

667 surface affected by Mg binding (see Figure 2 and discussion
 668 above).

669 These observations are consistent with the experimental data
 670 reported for exogenous addition of $A\beta(1-42)$ to bilayer
 671 models (POPC/POPS mixtures).⁵³ Comparing 2H and ^{31}P
 672 solid-state NMR of $A\beta(1-42)$ and $Cu-A\beta(1-42)$, a clear
 673 indication of the confinement of peptides around the head
 674 groups is shown. Peptide incorporation during the bilayer
 675 preparation, on the other hand, has more severe impact on
 676 NMR data and bilayer stability, irrespective of Cu addition.

677 **Effect of Peptide Addition to the DMPC Bilayer**
 678 **Structure.** The area per lipid as a function of temperature
 679 measured by REMD simulation (see above) and consistent
 680 with experimental data⁸¹ shows that the area per lipid increases
 681 with temperature. Therefore, most of the changes displayed in
 682 Table 3 are due to the lower T used in the CMD simulations of
 683 $A\beta$ /DMPC and $Cu-A\beta$ /DMPC ($T = 303$ K) compared to
 684 DMPC and Mg/DMPC ($T = 311$ K). The choice of $T = 303$ K
 685 is to compare these results to CMD simulations of $A\beta(1-42)$
 686 and $Cu-A\beta(1-42)$ in the absence of DMPC.⁵² Despite the
 687 more significant effect of peptide/DMPC interactions in the 10
 688 separated CMD than in REMD, the changes in the bilayer
 689 structural parameters (Table 3) are consistent with the
 690 experimental data⁵³ that show a small structural effect for the
 691 bilayer, when addition of both $A\beta(1-42)$ and $Cu-A\beta(1-42)$
 692 to the POPC/POPS bilayer is exogenous. On the other hand,
 693 the peptide incorporation has a more significant effect on the
 694 structure of DMPC head groups, as it discussed in the next
 695 subsections. As for bilayer thickness, in our simulations, we
 696 observe a few incorporated samples, but in all cases where
 697 peptide incorporation occurs, the thickness of the bilayer is not
 698 dramatically affected, compared to the case where the peptide
 699 is confined at the membrane surface. The change in area per
 700 lipid is, on the other hand, more significant for trajectory 1
 701 (61.6 Å²) compared to the average (60.6). This shows that
 702 peptide digs a little hollow, separating the lipid molecules one
 703 from each other, with no wide changes in the bilayer structure,
 704 like those emerging from the displacement of a lipid head
 705 group from the layer to the solvent.

706 The order parameters of hydrophobic DMPC chains (data
 707 not shown here) show a negligible effect of both $A\beta$ and $Cu-$
 708 $A\beta$ exogenous addition to DMPC. This is an expected effect
 709 because the penetration of the peptide into the bilayer is small
 710 (see Figure 5B).

711 **Effect of Peptide Addition to DMPC on Electrostatic**
 712 **Properties.** We extend the measure of the effects of
 713 interactions between the peptide and the DMPC head groups
 714 on the distribution of monovalent ions (K^+) on the two layers.

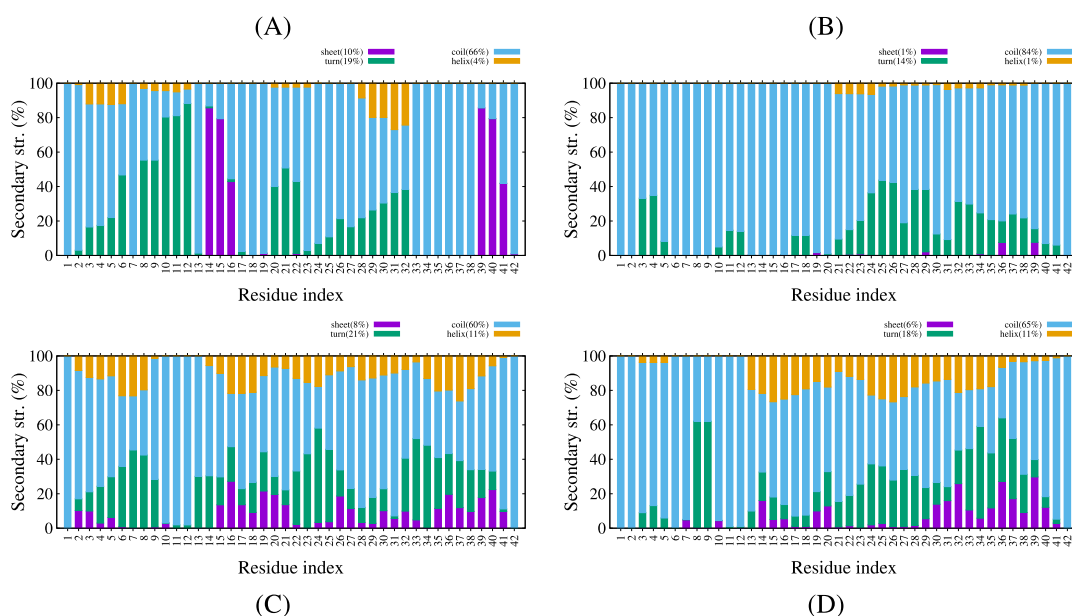


Figure 6. Secondary structure (see the [Methods](#) section for definition) as a function of residue in $A\beta$. Top: (A) $A\beta(1-42)$ and $Cu-A\beta(1-42)$ (B) without DMPC.⁵² Bottom: secondary structure averaged over 10 trajectories, $A\beta(1-42)/DMPC$ (C) and $Cu-A\beta(1-42)/DMPC$ (D).

715 Again, to better understand these effects, we analyze the
 716 different CMD trajectories. In [Figure S4](#) (see the Supporting
 717 Information), we compare the RDF for pairs involving P atoms
 718 in DMPC and atoms in the N-terminus of the peptide, N(Asp
 719 1) and Cu in, respectively, $A\beta/DMPC$ and $Cu-A\beta/DMPC$.
 720 For instance, comparing trajectories 1 and 2 for $A\beta/DMPC$
 721 and $Cu-A\beta/DMPC$, we notice that the more symmetric is the
 722 interaction between the peptide among the two layers (left
 723 panels), the more symmetric is the distribution of K^+ (right
 724 panels). It is also interesting to notice that the strong
 725 interaction of trajectory 1 for $A\beta/DMPC$ (see above) produces
 726 polarization of K^+ that is opposite to that produced by Mg^{2+}
 727 ([Figure S2A](#), black curve).

728 Effect of Cu and DMPC on the Peptide Structure.

729 Circular dichroism (CD) provides important experimental
 730 information about the change of the structure of $A\beta(1-42)$
 731 and $Cu-A\beta(1-42)$ when the peptides are added to the
 732 preformed bilayer.⁵³ When these experiments are performed at
 733 low peptide concentration (by using synchrotron radiation
 734 sources), aggregation phenomena are minimized during the
 735 measurements. These experiments show that the change of the
 736 structure of the peptide is minimal, both without and with Cu,
 737 when peptides are added to the bilayer. A more significant
 738 change occurs when peptides are incorporated during bilayer
 739 formation and, in the latter case, the addition of Cu is also
 740 affecting structural modification. In [Figure 6](#) we report the
 741 average secondary structure of the peptide, both without
 742 DMPC (top, data from ref 52) and with DMPC (bottom, this
 743 work). The data show that the effect of DMPC association on
 744 the peptide is, on average, small: there is only a significant
 745 increase in population of helical regions together with a
 746 spreading of the β -sheet content among residues. We notice
 747 that simulations with no membrane have been performed with
 748 a different force-field (AMBER FF99SB).

749 In [Table 4](#), we compare structural parameters averaged over
 750 10 trajectories, with those obtained for some selected
 751 trajectories, the latter showing the largest extent of association
 752 with DMPC. As for those trajectories that are more strongly
 753 interacting with the bilayer (especially trajectories 1 of $A\beta/$

DMPC and 8 of $Cu-A\beta/DMPC$), the helical content is
 754 significantly increased. This is an expected result because it is
 755 well known that the incorporation of $A\beta(1-40)$ into vesicles
 756 produces α -helical motifs in the peptide.⁸³ It must be noticed
 757 that when the peptide is embedded into the bilayer ($A\beta/$
 758 DMPC, traj. 1), there is an expansion of the peptide, while the
 759 association with the bilayer surface ($A\beta/DMPC$, traj. 5, $Cu-$
 760 $A\beta/DMPC$, traj. 8) induces significant compaction. The size
 761 and secondary structure of the peptide is, therefore,
 762 significantly modulated by the type of association when the
 763 latter occurs: electrostatic (strong interaction with bilayer
 764 surface) versus hydrophobic (penetration into the bilayer).
 765

The penetration of the peptide into the membrane increases,
 766 as expected, the helix content. The maximal percentage of helix
 767 is displayed by the trajectories where the penetration is deeper:
 768 trajectory 1 for $A\beta/DMPC$ and trajectory 8 for $Cu-A\beta/$
 769 DMPC, 15 and 20%, respectively ([Table 4](#)). This percentage is
 770 lower than that reported for $A\beta(1-42)$ in micelles on the basis
 771 of CD and NMR experiments in SDS⁸⁴ and in helix-inducing
 772 solvents.⁸⁵ The difference can be due to the partial
 773 achievement of peptide penetration in our simulation, where
 774 an exogenous addition is performed, compared to fully
 775 embedded $A\beta(1-42)$ in micelles, where the assembly is
 776 prepared starting with the components. Another possibility,
 777 which we cannot verify in this work, is limitations of force-field
 778 and sampling. It is known that conformational changes within
 779 the lipid bilayer require long simulation timescales, and only
 780 electrostatic interactions with the charged group of the
 781 membrane can abruptly affect the $A\beta(1-42)$ structure.¹⁵
 782

The number of intramolecular SBs is, on average, over the
 783 10 trajectories, not altered in the presence of DMPC with
 784 respect to the case of water solution ([Table 4](#)). The SB
 785 quantity increases when the association of the peptide with
 786 DMPC is more significant (trajectories 1 and 5 for $A\beta/DMPC$,
 787 trajectory 8 for $Cu-A\beta/DMPC$). The number of contacts
 788 between positively charged groups in $A\beta$ (see the [Methods](#)
 789 section) and P atoms, does not increase substantially, being
 790 always around 0.2, independently from the chosen trajectory
 791 (data not shown in tables). The number of contacts between
 792

793 negatively charged groups in the peptide and the ammonium
794 group in DMPC is always negligible because of the steric effect
795 of methyl groups attached to the N atom. These data indicate
796 that the extent of association between the peptide and
797 membrane is independent from the electrostatic interactions
798 between charged groups in the peptide and those with
799 opposite charge at the membrane surface. The charged head
800 groups in the membrane are, on average, not sufficient to
801 divert charged groups in the peptide from pre-existent SBs.

802 Further illustration of the type of interactions occurring in
803 the peptide/DMPC association can be obtained by examining
804 and comparing the final configurations of trajectories
805 characterized by a different behavior. We limit this comparison,
806 reported in Figure 7, to $A\beta$ /DMPC because the difference with
807 Cu- $A\beta$ /DMPC is, in this respect, marginal. The final
808 configuration in trajectory 2 (top) represents a typical weak
809 interaction between an almost-unperturbed $A\beta$ peptide and the
810 surface of DMPC. Trajectory 5 (middle) ends with
811 configurations significantly penetrating the membrane bilayer
812 but with interactions almost confined to the surface. Finally, in
813 trajectory 1, the peptide rapidly achieves the penetration of the
814 bilayer from the side of its C-terminus (bottom). In the latter
815 conditions, it can be noticed that the region of $A\beta$ crossing the
816 layer surface is small, separating the N-terminus (above the
817 surface) and the C-terminus (below the surface). This
818 configuration, again, represents the requirement of removing
819 the cross-talk between the N-terminus and the C-terminus
820 (exerted by the bending of N-terminus towards the C-
821 terminus) before a deeper penetration of the peptide into the
822 membrane from the side of the C-terminus. This configuration
823 is similar to that obtained by REMD of Cu- $A\beta$ /DMPC,
824 displaying the deepest penetration into the bilayer (Figure 4B),
825 with the main difference that the N-terminus is not partially
826 neutralized by Cu binding.

827 Further comparison between statistical properties in the
828 three different simulations represented with the snapshots
829 described above confirms the description of the force that is
830 exerted by the DMPC bilayer when the peptide is
831 incorporated. In the left panels of Figure 8, the probability
832 of inter-residue contacts (see the Methods section) is displayed
833 for trajectories 2 (top), 5 (middle), and 1 (bottom panels). In
834 the first case, there are almost no interactions between $A\beta(1-42)$
835 and DMPC because the number of $A\beta$ /DMPC contacts is
836 5. In trajectory 5, significant interactions of $A\beta(1-42)$ with the
837 bilayer surface are revealed by an increase in the number of
838 $A\beta$ /DMPC contacts to 13. Finally, in trajectory 1, the deepest
839 penetration of the peptide into the bilayer occurs, and the
840 number of contacts increases to 49. Again, trajectory 2 (top
841 panel) displays a typical behavior for an unperturbed $A\beta(1-42)$
842 peptide, where a weak cross-talk between many residues is
843 allowed by the structural disorder of the peptide. As already
844 observed for the monomeric $A\beta(1-42)$ peptide in water
845 solution, contacts are distributed among two domains, one N-
846 terminal and one C-terminal, as it is shown by the low
847 probability of contacts in the range of residues 20–26. In the
848 case of interactions confined to the DMPC bilayer surface
849 (trajectory 5, middle panel), we observe a conformational
850 freezing, displayed by an increase, with respect to the free
851 peptide, of highly populated contacts between residues far in
852 the sequence. Some of them involve Glu 22, Asp 23, and Lys
853 28, with these charged side chains interacting mostly with the
854 N-terminus and not between themselves. In the case of a
855 peptide that is more significantly embedded into the bilayer

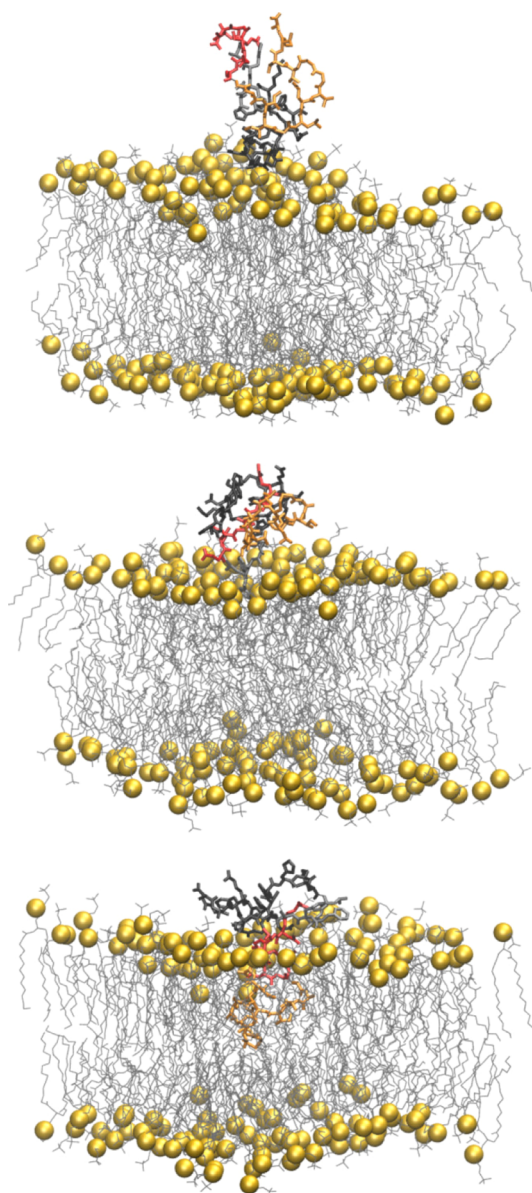


Figure 7. Final configurations of $A\beta$ /DMPC in trajectories 2 (top), 5 (middle), and 1 (bottom). Residues 1–16 are in black (segment S1 in Figure 8), 17–21 in gray (S2), 22–28 in red (S3), and 29–42 in blue (S4). The peptide is represented as bond sticks. P atoms in DMPC are represented as yellow spheres. The other DMPC atoms are represented as lines. Water molecules and ions are not displayed. Bond and atomic radii are arbitrary.

(trajectory 1, bottom panel), one notices the disappearance of
856 contacts within residues in the C-terminus and the extension of
857 the N-terminal domain up to Lys 28, with the void observed
858 for trajectory 2 (top) almost filled. This change in cross-talk is
859 induced by the formation of contacts between the C-terminus
860 and DMPC. In the right panels of the same figure, we display
861 the mass density for different atomic sets in $A\beta(1-42)$. S1 is
862 the N-terminus, S4 the C-terminus, while S2 is the hydro-
863 phobic segment, and S3 contains the charged residues involved
864 in one of the intramolecular SBs. When the peptide is out from
865 the bilayer (trajectory 2, top-right panel), only the N-terminus
866 (S1) is approaching the bilayer surface. The analysis of the
867 trajectories not displaying penetration into the bilayer (all
868 trajectories except 1 and 5, data not shown here) shows that 869

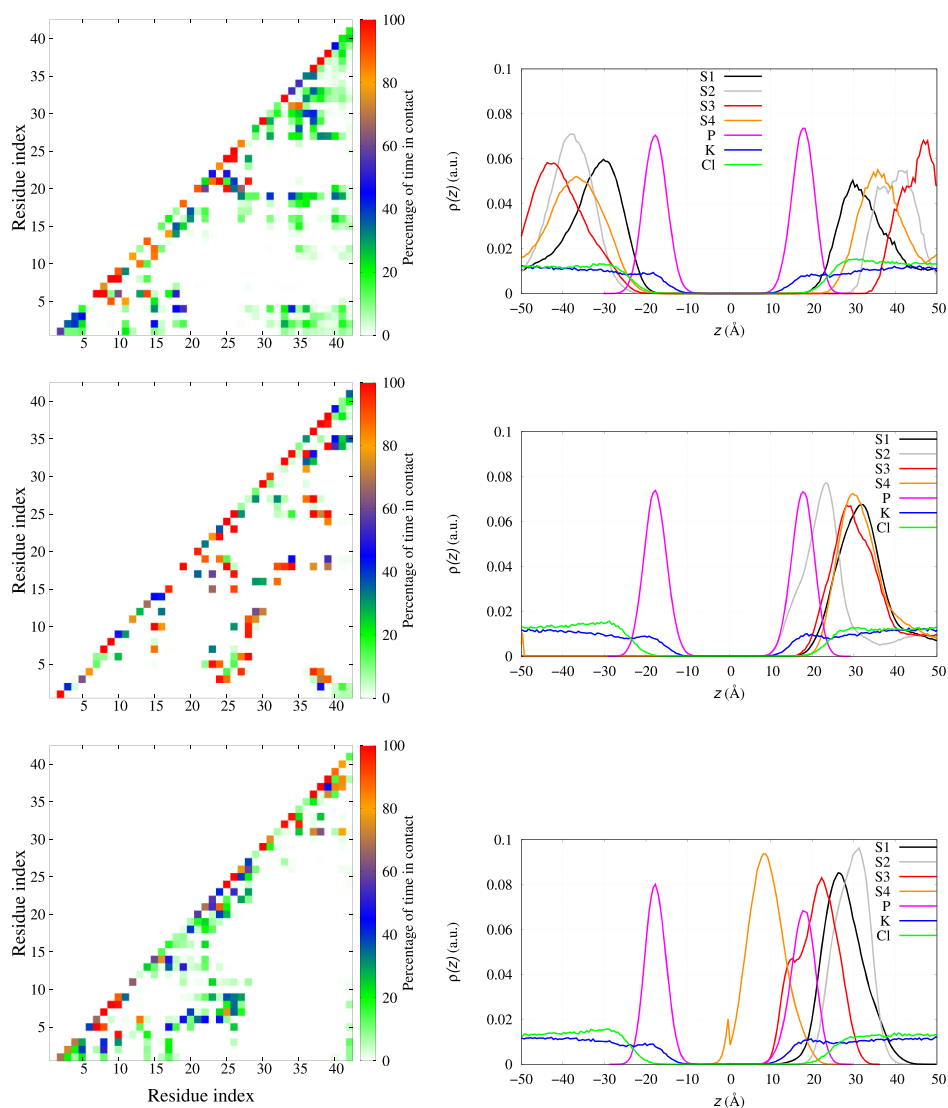


Figure 8. Probability, for $A\beta$ /DMPC, of inter-residue contacts (left panels, see the [Methods](#) section for details) and density of mass for different atomic sets as a function of the coordinate z along the bilayer normal (right panels): trajectory 2 (top); trajectory 5 (middle); trajectory 1 (bottom). S1 are residues 1–16, S2 17–21, S3 22–28, S4 29–42. The density of each component is divided by the number of atoms in each atomic set.

870 there is no preference among the different segments for weak
871 interactions with the bilayer surface. When a more significant
872 interaction with the bilayer surface occurs (trajectory 5,
873 middle-right panel), the hydrophobic segment S2 is projected
874 toward the bilayer because of stronger interactions among S3
875 and S1 (as shown in the middle-left panel). When the
876 penetration is deeper (trajectory 1, bottom-right panel), the S4
877 segment overtakes the layer of P atoms, with the latter
878 interacting with S3. Interestingly, in these conditions, the S2
879 segment is projected toward the water layer, thus allowing
880 interactions with other monomers nearby, especially if pre-
881 organized as in trajectory 5 (middle panel).

882 As for Cu- $A\beta$ /DMPC, 9 of 10 trajectories display the
883 behavior of $A\beta$ /DMPC in trajectory 2, while only trajectory 8
884 displays a pattern similar to trajectory 5 in $A\beta$ /DMPC.

885 The observations related to contacts, both defined as specific
886 SBs and generic inter-residue contacts, represent the process of
887 changing the cross-talk between domains that are polymorphic
888 in the free $A\beta(1-42)$ peptide. The interactions with the
889 charges on the surface of the membrane bilayer select

configurations that have low population in the DMPC- 890
unbound state, thus indicating a free energy barrier in the 891
process of peptide penetration through the bilayer surface. The 892
observation that peptide embedding into the membrane is a 893
rare event (1 trajectory over 10) shows that the structural 894
changes accompanying penetration are hindered by the 895
polymorphism that characterizes the monomeric $A\beta(1-42)$ 896
peptide. The Cu binding to $A\beta(1-40)$ enhances the spread of 897
configurations over polymorphic states in the monomeric 898
state,⁶¹ thus providing possible entropic explanation to the 899
question why Cu binding reduces the penetration of 900
monomers through the charged DMPC surface. 901

Again, we remind that this analysis is limited to peptide 902
monomers. 903

DISCUSSION

In previous works, we analyzed in detail the effect of Cu- 905
binding on the properties of $A\beta(1-42)$ peptide, both in 906
monomeric and dimeric states. Simulations of Cu-bound 907
monomers and dimers show that Cu-binding hinders the 908

909 formation of larger oligomers and amorphous aggregates, and
910 the latter is the final stable form of Cu- $A\beta(1-42)$ in water
911 solution.⁸⁶⁻⁸⁸ One major result of our simplified models for
912 monomers in water is that the interactions between the peptide
913 charged side chains and the water solvent are enhanced by the
914 dominant coordination mode of Cu observed in electron
915 paramagnetic resonance spectroscopy. This observation is
916 consistent with the longer lifetime observed for Cu- $A\beta(1-42)$
917 monomers compared to $A\beta(1-42)$ monomers, when the Cu/
918 $A\beta$ ratio is 1:1, that is, when all peptides are bound to Cu.⁸⁷
919 According to models of $A\beta(1-42)$ and Cu- $A\beta(1-42)$
920 nucleation kinetics, Cu binding, together with Zn-binding,
921 promotes $A\beta$ aggregation into amorphous particles, rather than
922 fibrils, because of the longer latency of soluble monomers and
923 oligomers bound to metal ions.⁸⁷

924 Therefore, by adding $A\beta(1-42)$ and Cu- $A\beta(1-42)$
925 monomers to DMPC, that is, a lipid bilayer with charged
926 head groups, the difference in organization of the charged side
927 chains is potentially important.

928 Our models of monomeric $A\beta(1-42)$ and Cu- $A\beta(1-42)$
929 in contact with the DMPC bilayer confirm the experimental
930 information that the exogenous addition to DMPC of these
931 peptides reveals peptide/membrane interactions that are
932 confined to the charged head groups of the bilayer. The
933 interactions between the peptide and the membrane are
934 concentrated in the head groups also in the few exceptions
935 where the peptides are significantly embedded into the
936 membrane bilayer. The exogenous addition of the peptide to
937 the membrane bilayer does not alter significantly the bilayer
938 structure when free divalent cations are either absent or bound
939 to the peptide. As for the $A\beta(1-42)$ peptide, this fact has been
940 already observed experimentally by means of spectroscopy and
941 diffraction studies.⁸⁹ Consistently, dramatic changes of
942 peptide/membrane interactions are observed at conditions
943 where the peptide is truncated to be more hydrophobic
944 [$A\beta(25-35)$] or forms fibril assemblies.^{89,90}

945 The picture of $A\beta$ monomers floating over the membrane
946 surface is consistent with other observations reported in the
947 literature. A recent FRET experimental work⁴ describes the
948 strong interactions among growing fibrils and the DOPC
949 membrane, modelled as a lipid vesicle. The same study
950 confirms that monomers do not directly bind the lipid bilayer,
951 as already observed in previous studies.

952 As for the impact on oligomer formation, our results point
953 out the possible role of charged groups of the bilayer in
954 organizing monomers into oligomers. Indeed, several simu-
955 lations showed that a strong association between $A\beta$ and
956 zwitterionic and charged membranes occurs starting from
957 tetrameric $A\beta$ assemblies.¹⁵ Because it is known that the lag-
958 time of monomers associated to Cu is larger than that of Cu-
959 free $A\beta$ when in the water solvent,⁸⁷ it is not surprising that the
960 DMPC association with $A\beta(1-42)$ in the absence of divalent
961 cations does not decrease the chance of intermonomer
962 contacts compared to the water solution. The bilayer-water
963 interface, when the bilayer has charged groups on the surface,
964 exerts mild attraction for $A\beta(1-42)$, thus decreasing the
965 freedom of monomers by reducing the space dimensionality.
966 Conversely, at the oligomeric level, the bilayer surface can
967 assist the formation of larger oligomers and protofibrils. This
968 type of association has been observed in models of preformed
969 protofibrils interacting with lipid bilayers.¹⁴

970 We notice here that in ss-NMR experiments, the effect of the
971 addition of free Cu^{2+} and Zn^{2+} ions on the membrane

properties is more dramatic than in the presence of the $A\beta$ 972
peptide.⁵³ Similar strong effects have been observed both 973
experimentally and computationally for free Ca^{2+} ions,⁴¹⁻⁴³ 974
and Mg and Cu divalent cations are even smaller than Ca^{2+} in 975
size. For the first time, we show in this study that the $A\beta$ - 976
bound Cu^{2+} ion does not exert strong perturbation on the 977
membrane exerted by a free divalent ion. Indeed, the effect of 978
the Cu- $A\beta$ monomer on the membrane is weaker than that of 979
the more charged $A\beta$ peptide. 980

Therefore, the formation of the Cu- $A\beta$ complex before 981
eventual incorporation into the membrane and before an 982
increase in peptide concentration appears as protection against 983
membrane destabilization and oxidation. This hypothesis is 984
confirmed using the NMR experiments performed with the 985
 $A\beta(25-35)$ peptide, both without and with Cu.^{54,89} Because 986
the N-truncated peptide does not bind Cu, the addition of Cu 987
to the system has an effect on the bilayer that is similar to that 988
of free Cu. 989

990 ■ CONCLUSIONS

We perturbed an atomistic model of the DMPC bilayer, 991
representing a very crude approximation of a portion of a 992
common cellular membrane, with a single divalent cation 993
(Mg^{2+}) and with Cu-free and Cu-loaded amyloid- β peptides of 994
42 amino acid residues in the monomeric form. 995

All the data reported in our simulations represent important 996
structural and electrostatic changes of the bilayer when a single 997
divalent cation interacts with the phosphate groups of DMPC. 998
On the other hand, the presence of the peptide represents a 999
floating molecule mildly interacting with the bilayer surface 1000
and well suited to sequester divalent cations, in this case, Cu^{2+} . 1001
The model clearly depicts the possible protective role of the 1002
amyloid- $\beta(1-42)$ peptide in avoiding interactions between 1003
 Cu^{2+} and the membrane. 1004

The model has many limitations. Beyond the limitations in 1005
the size and number of components, that are common to 1006
applications of atomistic models, there is the lack of working 1007
approximations to interactions between an ion like Cu^{2+} , with 1008
available 3d orbitals, and molecules providing a plethora of 1009
possible ligand atoms, like phosphate, carboxylate, imidazole, 1010
and carbonyl groups, not to mention deprotonated amide 1011
backbone nitrogen that are known to bind Cu^{2+} at 1012
physiological pH. There have been applications of modified 1013
nonbonding models for Cu^{2+} and Zn^{2+} cations that maintain 1014
pre-organized binding sites⁹¹ but are limited in describing the 1015
exchange of cations between imidazole and carboxylate side 1016
chains. These limitations will be eventually removed using 1017
polarizable and reactive force-fields that are not yet available. 1018

The investigation of events occurring when the concen- 1019
tration of the peptide increases are the future perspective of 1020
this study. However, the type of weak interactions of the 1021
peptide with DMPC shows that modulation of interpeptide 1022
electrostatic interactions are likely changing the picture 1023
describing the behavior of monomers, where intramolecular 1024
SBs are found to be particularly stable. The assembly of several 1025
monomers into oligomers, especially when loaded with Cu^{2+} , is 1026
likely affecting the surface of the bilayer. Then, as expected, the 1027
increase in concentration of Cu- $A\beta(1-42)$ close to a 1028
biological membrane becomes a possible crucial event 1029
destabilizing the neuron membrane. The increase in the 1030
turnover of Cu- $A\beta$ monomers or dimers, possibly because of 1031
self-oxidation (the latter enhanced in dimers), can also 1032
contribute to membrane protection. 1033

1034 ■ ASSOCIATED CONTENT

1035 ■ Supporting Information

1036 The Supporting Information is available free of charge at
1037 <https://pubs.acs.org/doi/10.1021/acs.jpcc.0c00771>.

1038 Description of the umbrella sampling method, lipid acyl
1039 chain order parameters, and rmsd (PDF)

1040 Initial coordinates for peptides divalent cations and the
1041 DMPC bilayer used in the reported simulations (ZIP)

1042 ■ AUTHOR INFORMATION

1043 Corresponding Authors

1044 Giovanni La Penna – National Research Council of Italy
1045 (CNR), Institute for Chemistry of Organometallic Compounds
1046 (ICCOM), 50019 Florence, Italy; National Institute for
1047 Nuclear Physics (INFN), Section of Roma-Tor Vergata, 00186
1048 Roma, Italy; orcid.org/0000-0002-8619-4867;
1049 Email: giovanni.lapenna@cnr.it

1050 Mai Suan Li – Institute of Physics, Polish Academy of Sciences,
1051 02-668 Warsaw, Poland; orcid.org/0000-0001-7021-7916;
1052 Email: masli@ifpan.edu.pl

1053 Authors

1054 Dinh Quoc Huy Pham – Institute of Physics, Polish Academy of
1055 Sciences, 02-668 Warsaw, Poland

1056 Pawel Krupa – Institute of Physics, Polish Academy of Sciences,
1057 02-668 Warsaw, Poland; orcid.org/0000-0002-9710-7837

1058 Hoang Linh Nguyen – Institute for Computational Science and
1059 Technology, 721400 Ho Chi Minh City, Vietnam

1060 Complete contact information is available at:

1061 <https://pubs.acs.org/doi/10.1021/acs.jpcc.0c00771>

1062 Notes

1063 The authors declare no competing financial interest.

1064 ■ ACKNOWLEDGMENTS

1065 The work was supported by Narodowe Centrum Nauki in
1066 Poland (grant no. 2015/19/B/ST4/02721); Department of
1067 Science and Technology (Ho Chi Minh City, Vietnam);
1068 PLGrid Infrastructure (Poland); and the bilateral project
1069 Cnr(I)-PAN(PL) “The role of copper ions in neurodegenera-
1070 tion: molecular models”.

1071 ■ REFERENCES

- 1072 (1) Blennow, K.; de Leon, M. J.; Zetterberg, H. Alzheimer’s Disease.
1073 *Lancet* **2006**, *368*, 387–403.
- 1074 (2) Müller, U. C.; Deller, T. Editorial: The Physiological Functions
1075 of the APP Gene Family. *Front. Mol. Neurosci.* **2017**, *10*, 334.
- 1076 (3) Kummer, M. P.; Heneka, M. T. Truncated and Modified
1077 Amyloid-beta Species. *Alzheimer’s Res. Ther.* **2014**, *6*, 28–36.
- 1078 (4) Lindberg, D. J.; Wesén, E.; Björkeröth, J.; Rocha, S.; Esbjörner,
1079 E. K. Lipid Membranes Catalyse the Fibril Formation of the Amyloid-
1080 β (1–42) Peptide through Lipid-fibril Interactions that Reinforce
1081 Secondary Pathways. *Biochim. Biophys. Acta, Biomembr.* **2017**, *1859*,
1082 1921–1929.
- 1083 (5) Mucke, L.; Masliah, E.; Yu, G.-Q.; Mallory, M.; Rockenstein, E.
1084 M.; Tatsuno, G.; Hu, K.; Kholodenko, D.; Johnson-Wood, K.;
1085 McConlogue, L. High-Level Neuronal Expression of A β 1–42 in Wild-
1086 Type Human Amyloid Protein Precursor Transgenic Mice:
1087 Synaptotoxicity without Plaque Formation. *J. Neurosci.* **2000**, *20*,
1088 4050–4058.
- 1089 (6) Evangelisti, E.; Cascella, R.; Becatti, M.; Marrazza, G.; Dobson,
1090 C. M.; Chiti, F.; Stefani, M.; Cecchi, C. Binding Affinity of Amyloid
1091 Oligomers to Cellular Membranes is a Generic Indicator of Cellular

Dysfunction in Protein Misfolding Diseases. *Sci. Rep.* **2016**, *6*, 32721–
1092 32734. 1093

(7) Niu, Z.; Zhang, Z.; Zhao, W.; Yang, J. Interactions between
1094 Amyloid- β Peptide and Lipid Membranes. *Biochim. Biophys. Acta*,
1095 *Biomembr.* **2018**, *1860*, 1663–1669. 1096

(8) Kepp, K. P. Alzheimer’s Disease Due to Loss of Function: A
1097 New Synthesis of the Available Data. *Prog. Neurobiol.* **2016**, *143*, 36–
1098 60. 1099

(9) Marrink, S. J.; Corradi, V.; Souza, P. C. T.; Ingólfsson, H. I.;
1100 Tieleman, D. P.; Sansom, M. S. P. Computational Modeling of
1101 Realistic Cell Membranes. *Chem. Rev.* **2019**, *119*, 6184–6226. 1102

(10) Lemkul, J. A.; Bevan, D. R. A Comparative Molecular
1103 Dynamics Analysis of the Amyloid β -peptide in a Lipid Bilayer.
1104 *Arch. Biochem. Biophys.* **2008**, *470*, 54–63. 1105

(11) Lockhart, C.; Klimov, D. K. Alzheimer’s A β 10–40 Peptide Binds
1106 and Penetrates DMPC Bilayer: An Isobaric-Isothermal Replica
1107 Exchange Molecular Dynamics Study. *J. Phys. Chem. B* **2014**, *118*,
1108 2638–2648. 1109

(12) Friedman, R.; Pellarin, R.; Caflish, A. Amyloid Aggregation on
1110 Lipid Bilayers and Its Impact on Membrane Permeability. *J. Mol. Biol.*
1111 **2009**, *387*, 407–415. 1112

(13) Liu, L.; Hyeon, C. Contact Statistics Highlight Distinct
1113 Organizing Principles of Proteins and RNA. *Biophys. J.* **2016**, *110*,
1114 2320–2327. 1115

(14) Tofoleanu, F.; Buchete, N.-V. Molecular Interactions of
1116 Alzheimer’s A β Protofilaments with Lipid Membranes. *J. Mol. Biol.*
1117 **2012**, *421*, 572–586. 1118

(15) Poojari, C.; Kukul, A.; Strodel, B. How the Amyloid-beta
1119 Peptide and Membranes Affect each Other: An Extensive Simulation
1120 Study. *Biochim. Biophys. Acta, Biomembr.* **2013**, *1828*, 327–339. 1121

(16) Tofoleanu, F.; Brooks, B. R.; Buchete, N.-V. Modulation of
1122 Alzheimer’s A β Protofilament-Membrane Interactions by Lipid
1123 Headgroups. *ACS Chem. Neurosci.* **2015**, *6*, 446–455. 1124

(17) Brown, A. M.; Bevan, D. R. Molecular Dynamics Simulations of
1125 Amyloid β -Peptide(1–42): Tetramer Formation and Membrane
1126 Interactions. *Biophys. J.* **2016**, *111*, 937–949. 1127

(18) Press-Sandler, O.; Miller, Y. Molecular Mechanisms of
1128 Membrane-associated Amyloid Aggregation: Computational Perspec-
1129 tive and Challenges. *Biochim. Biophys. Acta, Biomembr.* **2018**, *1860*,
1130 1889–1905. 1131

(19) Friedman, R. Membrane-Ion Interactions. *J. Membr. Biol.* **2018**,
1132 *251*, 453–460. 1133

(20) Ackerman, C. M.; Chang, C. J. Copper Signaling in the Brain
1134 and Beyond. *J. Biol. Chem.* **2018**, *293*, 4628–4635. 1135

(21) Hartter, D. E.; Barnea, A. Evidence for Release of Copper in the
1136 Brain: Depolarization-induced Release of Newly Taken-up ^{67}Cu .
1137 *Synapse* **1988**, *2*, 412–415. 1138

(22) Vassallo, N.; Herms, J. Cellular Prion Protein Function in
1139 Copper Homeostasis and Redox Signalling at the Synapse. *J.*
1140 *Neurochem.* **2003**, *86*, 538–544. 1141

(23) Wild, K.; August, A.; Pietrzik, C. U.; Kins, S. Structure and
1142 Synaptic Function of Metal Binding to the Amyloid Precursor Protein
1143 and its Proteolytic Fragments. *Front. Mol. Neurosci.* **2017**, *10*, 21–32. 1144

(24) Rae, T. D.; Schmidt, P. J.; Pufahl, R. A.; Culotta, V. C.;
1145 O’Halloran, T. V. Undetectable Intracellular Free Copper: The
1146 Requirement of a Copper Chaperone for Superoxide Dismutase.
1147 *Science* **1999**, *284*, 805–808. 1148

(25) Kepp, K. P. Alzheimer’s Disease: How Metal Ions Define β -
1149 amyloid Function. *Coord. Chem. Rev.* **2017**, *351*, 127–159. 1150

(26) Multhaup, G.; Schlicksupp, A.; Hesse, L.; Beher, D.; Ruppert,
1151 T.; Masters, C. L.; Beyreuther, K. The Amyloid Precursor Protein of
1152 Alzheimer’s Disease in the Reduction of Copper(II) to Copper(I).
1153 *Science* **1996**, *271*, 1406–1409. 1154

(27) Strausak, D.; Mercer, J. F. B.; Dieter, H. H.; Stremmel, W.;
1155 Multhaup, G. Copper in Disorders with Neurological Symptoms:
1156 Alzheimer’s, Menkes, and Wilson Diseases. *Brain Res. Bull.* **2001**, *55*,
1157 175–185. 1158

(28) Gaggelli, E.; Kozłowski, H.; Valensin, D.; Valensin, G. Copper
1159 Homeostasis and Neurodegenerative Disorders (Alzheimer’s, Prion,
1160

- 1161 and Parkinson's Diseases and Amyotrophic Lateral Sclerosis). *Chem.*
1162 *Rev.* **2006**, *106*, 1995–2044.
- 1163 (29) Ohba, S.; Hiramatsu, M.; Edamatsu, R.; Mori, I.; Mori, A.
1164 Metal Ions Affect Neuronal Membrane Fluidity of Rat Cerebral
1165 Cortex. *Neurochem. Res.* **1994**, *19*, 237–241.
- 1166 (30) Suwalsky, M.; Ungerer, B.; Quevedo, L.; Aguilar, F.;
1167 Sotomayor, C. P. Cu²⁺ Ions Interact with Cell Membranes. *J.*
1168 *Inorg. Biochem.* **1998**, *70*, 233–238.
- 1169 (31) García, J. J.; Martínez-Ballarín, E.; Millán-Plano, S.; Allué, J. L.;
1170 Albendea, C.; Fuentes, L.; Escanero, J. F. Effects of Trace Elements on
1171 Membrane Fluidity. *J. Trace Elem. Med. Biol.* **2005**, *19*, 19–22.
- 1172 (32) Jiang, X.; Zhang, J.; Zhou, B.; Li, P.; Hu, X.; Zhu, Z.; Tan, Y.;
1173 Chang, C.; Lü, J.; Song, B. Anomalous Behavior of Membrane
1174 Fluidity Caused by Copper-copper Bond Coupled Phospholipids. *Sci.*
1175 *Rep.* **2018**, *8*, 14093.
- 1176 (33) Quist, A.; Doudevski, I.; Lin, H.; Azimova, R.; Ng, D.;
1177 Frangione, B.; Kagan, B.; Ghiso, J.; Lal, R. Amyloid Ion Channels: A
1178 Common Structural Link for Protein-misfolding Disease. *Proc. Natl.*
1179 *Acad. Sci. U.S.A.* **2005**, *102*, 10427–10432.
- 1180 (34) Di Scala, C.; Chahinian, H.; Yahji, N.; Garmy, N.; Fantini, J.
1181 Interaction of Alzheimer's β -Amyloid Peptides with Cholesterol:
1182 Mechanistic Insights into Amyloid Pore Formation. *Biochemistry*
1183 **2014**, *53*, 4489–4502.
- 1184 (35) Reybier, K.; Ayala, S.; Alies, B.; Rodrigues, J. V.; Bustos-
1185 Rodriguez, S.; La Penna, G.; Collin, F.; Gomes, C. M.; Hureau, C.;
1186 Faller, P. Free Superoxide is an Intermediate in the Production of
1187 H₂O₂ by Copper(I) α - β Peptide and O₂. *Angew. Chem., Int. Ed.*
1188 **2016**, *55*, 1085–1089.
- 1189 (36) La Penna, G.; Li, M. S. Towards a High-throughput Modelling
1190 of Copper Reactivity Induced by Structural Disorder in Amyloid
1191 Peptides. *Chem.—Eur. J.* **2018**, *24*, 5259–5270.
- 1192 (37) Lynch, T.; Cherny, R.; Bush, A. I. Oxidative Processes in
1193 Alzheimer's Disease: the Role of $\text{A}\beta$ -metal Interactions. *Exp. Gerontol.*
1194 **2000**, *35*, 445–451.
- 1195 (38) Perry, G.; Sayre, L. M.; Atwood, C. S.; Castellani, R. J.; Cash, A.
1196 D.; Rottkamp, C. A.; Smith, M. A. The Role of Iron and Copper in
1197 the Aetiology of Neurodegenerative Disorders. *CNS Drugs* **2002**, *16*,
1198 339–352.
- 1199 (39) Bagheri, S.; Squitti, R.; Haertlé, T.; Siotto, M.; Saboury, A. A.
1200 Role of Copper in the Onset of Alzheimer's Disease Compared to
1201 Other Metals. *Front. Aging Neurosci.* **2018**, *9*, 446–460.
- 1202 (40) Widomska, J.; Raguz, M.; Subczynski, W. K. Oxygen
1203 Permeability of the Lipid Bilayer Membrane Made of Calf Lens
1204 Lipids. *Biochim. Biophys. Acta, Biomembr.* **2007**, *1768*, 2635–2645.
- 1205 (41) Javanainen, M.; Melcrová, A.; Magarkar, A.; Jurkiewicz, P.; Hof,
1206 M.; Jungwirth, P.; Martinez-Seara, H. Two Cations, Two Mecha-
1207 nisms: Interactions of Sodium and Calcium with Zwitterionic Lipid
1208 Membranes. *Chem. Commun.* **2017**, *53*, 5380–5383.
- 1209 (42) Bilkova, E.; Pleskot, R.; Rissanen, S.; Sun, S.; Czogalla, A.;
1210 Cwiklik, L.; Róg, T.; Vattulainen, I.; Cremer, P. S.; Jungwirth, P.; et al.
1211 Calcium Directly Regulates Phosphatidylinositol 4,5-Bisphosphate
1212 Headgroup Conformation and Recognition. *J. Am. Chem. Soc.* **2017**,
1213 *139*, 4019–4024.
- 1214 (43) Melcr, J.; Martinez-Seara, H.; Nencini, R.; Kolafa, J.; Jungwirth,
1215 P.; Ollila, O. H. S. Accurate Binding of Sodium and Calcium to a
1216 POPC Bilayer by Effective Inclusion of Electronic Polarization. *J.*
1217 *Phys. Chem. B* **2018**, *122*, 4546–4557.
- 1218 (44) Nguyen, H. T.; Hori, N.; Thirumalai, D. Theory and
1219 Simulations for RNA Folding in Mixtures of Monovalent and
1220 Divalent Cations. *Proc. Natl. Acad. Sci. U.S.A.* **2019**, *116*, 21022–
1221 21030.
- 1222 (45) Miller, Y.; Ma, B.; Nussinov, R. Metal Binding Sites in Amyloid
1223 Oligomers: Complexes and Mechanisms. *Coord. Chem. Rev.* **2012**,
1224 *256*, 2245–2252.
- 1225 (46) Wineman-Fisher, V.; Bloch, D. N.; Miller, Y. Challenges in
1226 Studying the Structures of Metal-amyloid Oligomers Related to Type
1227 2 Diabetes, Parkinson's Disease, and Alzheimer's Disease. *Coord.*
1228 *Chem. Rev.* **2016**, *327–328*, 20–26.
- (47) Duarte, F.; Bauer, P.; Barrozo, A.; Amrein, B. A.; Purg, M.;
Åqvist, J.; Kamerlin, S. C. L. Force Field Independent Metal
Parameters Using a Nonbonded Dummy Model. *J. Phys. Chem. B*
2014, *118*, 4351–4362.
- (48) La Penna, G.; Chelli, R. Structural Insights into the
Osteopontin-Aptamer Complex by Molecular Dynamics Simulations.
Front. Chem. **2018**, *6*, 1–11.
- (49) Drew, S. C.; Masters, C. L.; Barnham, K. J. Alanine-2 Carbonyl
is an Oxygen Ligand in Cu²⁺ Coordination of Alzheimer's Disease
Amyloid- β Peptide: Relevance to N-terminally Truncated Forms. *J.*
Am. Chem. Soc. **2009**, *131*, 8760–8761.
- (50) Dorlet, P.; Gambarelli, S.; Faller, P.; Hureau, C. Pulse EPR
spectroscopy Reveals the Coordination Sphere of Copper(II) Ions in
the 1-16 Amyloid- β Peptide: A Key Role of the First two N-terminus
Residues. *Angew. Chem., Int. Ed.* **2009**, *48*, 9273–9276.
- (51) Kim, D.; Kim, N. H.; Kim, S. H. 34 GHz Pulsed ENDOR
Characterization of the Copper Coordination of an Amyloid β
Peptide Relevant to Alzheimer's Disease. *Angew. Chem., Int. Ed.* **2013**,
52, 1139–1142.
- (52) Huy, P. D. Q.; Vuong, Q. V.; La Penna, G.; Faller, P.; Li, M. S.
Impact of Cu(II) Binding on Structures and Dynamics of $\text{A}\beta$ 42
Monomer and Dimer: Molecular Dynamics Study. *ACS Chem.*
Neurosci. **2016**, *7*, 1348–1363.
- (53) Lau, T.-L.; Ambroggio, E. E.; Tew, D. J.; Cappai, R.; Masters,
C. L.; Fidelio, G. D.; Barnham, K. J.; Separovic, F. Amyloid- β Peptide
Disruption of Lipid Membranes and the Effect of Metal Ions. *J. Mol.*
Biol. **2006**, *356*, 759–770.
- (54) Lau, T.-L.; Gehman, J. D.; Wade, J. D.; Perez, K.; Masters, C.
L.; Barnham, K. J.; Separovic, F. Membrane Interactions and the
Effect of Metal Ions of the Amyloidogenic Fragment $\text{A}\beta$ (25-35) in
Comparison to $\text{A}\beta$ (1-42). *Biochim. Biophys. Acta, Biomembr.* **2007**,
1768, 2400–2408.
- (55) Goldberg, M.; De Pittà, M.; Volman, V.; Berry, H.; Ben-Jacob,
E. Nonlinear Gap Junctions Enable Long-Distance Propagation of
Pulsating Calcium Waves in Astrocyte Networks. *PLoS Comput. Biol.*
2010, *6*, No. e1000909.
- (56) Case, D.; Betz, R.; Cerutti, D.; Cheatham, T., III; Darden, T.;
Duke, R. E.; Giese, T.; Gohlke, H.; Goetz, A.; Homeyer, N.; et al.
AMBER 2016; University of California at San Francisco: San
Francisco, USA, 2016.
- (57) Maier, J. A.; Martinez, C.; Kasavajhala, K.; Wickstrom, L.;
Hauser, K. E.; Simmerling, C. ff14SB: Improving the Accuracy of
Protein Side Chain and Backbone Parameters from ff99SB. *J. Chem.*
Theory Comput. **2015**, *11*, 3696–3713.
- (58) Jorgensen, W. L.; Chandrasekhar, J.; Madura, J. D.; Impey, R.
W.; Klein, M. L. Comparison of Simple Potential Functions for
Simulating Liquid Water. *J. Chem. Phys.* **1983**, *79*, 926–935.
- (59) Dickson, C. J.; Madej, B. D.; Skjevik, A. A.; Betz, R. M.; Teigen,
K.; Gould, I. R.; Walker, R. C. Lipid14: The Amber Lipid Force Field.
J. Chem. Theory Comput. **2014**, *10*, 865–879.
- (60) Hornak, V.; Abel, R.; Okur, A.; Strockbine, B.; Roitberg, A.;
Simmerling, C. Comparison of Multiple Amber Force Fields and
Development of Improved Protein Backbone Parameters. *Proteins:*
Struct., Funct., Bioinf. **2006**, *65*, 712–725.
- (61) Pham, D. Q. H.; Li, M. S.; La Penna, G. Copper Binding
Induces Polymorphism in Amyloid- β Peptide: Results of Computa-
tional Models. *J. Phys. Chem. B* **2018**, *122*, 7243–7252.
- (62) Somavarapu, A. K.; Kepp, K. P. The Dependence of Amyloid- β
Dynamics on Protein Force Fields and Water Models. *ChemPhysChem*
2015, *16*, 3278–3289.
- (63) Carballo-Pacheco, M.; Strodel, B. Comparison of Force Fields
for Alzheimer's $\text{A}\beta$ 42: A Case Study for Intrinsically Disordered
Proteins. *Protein Sci.* **2017**, *26*, 174–185.
- (64) Liao, Q.; Owen, M. C.; Olubiyi, O. O.; Barz, B.; Strodel, B.
Conformational Transitions of the Amyloid- β Peptide Upon Copper-
(II) Binding and pH Changes. *Isr. J. Chem.* **2017**, *57*, 771–784.
- (65) Liao, Q.; Owen, M. C.; Bali, S.; Barz, B.; Strodel, B. $\text{A}\beta$ Under
Stress: the Effects of Acidosis, Cu²⁺-binding, and Oxidation on
Amyloid β -peptide Dimers. *Chem. Commun.* **2018**, *54*, 7766–7769.

- 1298 (66) Man, V. H.; He, X.; Derreumaux, P.; Ji, B.; Xie, X.-Q.; Nguyen,
1299 P. H.; Wang, J. Effects of All-Atom Molecular Mechanics Force Fields
1300 on Amyloid Peptide Assembly: The Case of A β (16-22) Dimer. *J.*
1301 *Chem. Theory Comput.* **2019**, *15*, 1440–1452.
- 1302 (67) Krupa, P.; Huy, P. D. Q.; Li, M. S. Properties of Monomeric
1303 A β 42 Probed by Different Sampling Methods and Force Fields: Role
1304 of Energy Components. *J. Chem. Phys.* **2019**, *151*, 055101–055114.
- 1305 (68) Bayly, C. I.; Cieplak, P.; Cornell, W.; Kollman, P. A. A Well-
1306 behaved Electrostatic Potential Based Method Using Charge
1307 Restraints for Deriving Atomic Charges: the RESP Model. *J. Phys.*
1308 *Chem.* **1993**, *97*, 10269–10280.
- 1309 (69) Cornell, W. D.; Cieplak, P.; Bayly, C. I.; Kollman, P. A.
1310 Application of RESP Charges to Calculate Conformational Energies,
1311 Hydrogen Bond Energies, and Free Energies of Solvation. *J. Am.*
1312 *Chem. Soc.* **1993**, *115*, 9620–9631.
- 1313 (70) Comba, P.; Remenyi, R. A New Molecular Mechanics Force
1314 Field for the Oxidized Form of Blue Copper Proteins. *J. Comput.*
1315 *Chem.* **2002**, *23*, 697–705.
- 1316 (71) Wu, X.; Brooks, B. R. Self-guided Langevin Dynamics
1317 Simulation Method. *Chem. Phys. Lett.* **2003**, *381*, 512–518.
- 1318 (72) Ryckaert, J.-P.; Ciccotti, G.; Berendsen, H. J. C. Numerical
1319 Integration of the Cartesian Equations of Motion with Constraints:
1320 Molecular Dynamics of n-alkanes. *J. Comput. Phys.* **1977**, *23*, 327–
1321 341.
- 1322 (73) Darden, T.; York, D.; Pedersen, L. Particle Mesh Ewald: An N-
1323 log(N) Method for Ewald Sums in Large Systems. *J. Chem. Phys.*
1324 **1993**, *98*, 10089–10092.
- 1325 (74) Weiser, J.; Shenkin, P. S.; Still, W. C. Approximate Atomic
1326 Surfaces from Linear Combinations of Pairwise Overlaps (LCPO). *J.*
1327 *Comput. Chem.* **1999**, *20*, 217–230.
- 1328 (75) Levine, Z. A.; Venable, R. M.; Watson, M. C.; Lerner, M. G.;
1329 Shea, J.-E.; Pastor, R. W.; Brown, F. L. H. Determination of
1330 Biomembrane Bending Moduli in Fully Atomistic Simulations. *J. Am.*
1331 *Chem. Soc.* **2014**, *136*, 13582–13585.
- 1332 (76) Watson, M. C.; Penev, E. S.; Welch, P. M.; Brown, F. L. H.
1333 Thermal Fluctuations in Shape, Thickness, and Molecular Orientation
1334 in Lipid Bilayers. *J. Chem. Phys.* **2011**, *135*, 244701–244723.
- 1335 (77) Marcus, Y. Thermodynamics of Solvation of Ions. Part 5. Gibbs
1336 Free Energy of Hydration at 298.15 K. *J. Chem. Soc., Faraday Trans.*
1337 **1991**, *87*, 2995–2999.
- 1338 (78) Tepper, H. L.; Voth, G. A. Mechanisms of Passive Ion
1339 Permeation through Lipid Bilayers: Insights from Simulations. *J. Phys.*
1340 *Chem. B* **2006**, *110*, 21327–21337.
- 1341 (79) Khavrutskii, I. V.; Gorfe, A. A.; Lu, B.; McCammon, J. A. Free
1342 Energy for the Permeation of Na⁺ and Cl⁻ Ions and Their Ion-Pair
1343 through a Zwitterionic Dimyristoyl Phosphatidylcholine Lipid Bilayer
1344 by Umbrella Integration with Harmonic Fourier Beads. *J. Am. Chem.*
1345 *Soc.* **2009**, *131*, 1706–1716.
- 1346 (80) Vorobyov, I.; Olson, T. E.; Kim, J. H.; Koeppe, R. E.; Andersen,
1347 O. S.; Allen, T. W. Ion-Induced Defect Permeation of Lipid
1348 Membranes. *Biophys. J.* **2014**, *106*, 586–597.
- 1349 (81) Kučerka, N.; Nieh, M.-P.; Katsaras, J. Fluid Phase Lipid Areas
1350 and Bilayer Thicknesses of Commonly Used Phosphatidylcholines as
1351 a Function of Temperature. *Biochim. Biophys. Acta, Biomembr.* **2011**,
1352 *1808*, 2761–2771.
- 1353 (82) López, C. A.; Unkefer, C. J.; Swanson, B. I.; Swanson, J. M. J.;
1354 Gnanakaran, S. Membrane Perturbing Properties of Toxin Myco-
1355 lactone from *Mycobacterium ulcerans*. *PLoS Comput. Biol.* **2018**, *14*,
1356 No. e1005972.
- 1357 (83) Jarvet, J.; Danielsson, J.; Damberg, P.; Oleszczuk, M.; Gräslund,
1358 A. Positioning of the Alzheimer A β (1-40) Peptide in SDS Micelles
1359 Using NMR and Paramagnetic Probes. *J. Biomol. NMR* **2007**, *39*, 63–
1360 72.
- 1361 (84) Shao, H.; Jao, S.-c.; Ma, K.; Zagorski, M. G. Solution Structures
1362 of Micelle-bound Amyloid β -(1-40) and β -(1-42) Peptides of
1363 Alzheimer's Disease. *J. Mol. Biol.* **1999**, *285*, 755–773.
- 1364 (85) Crescenzi, O.; Tomaselli, S.; Guerrini, R.; Salvadori, S.; D'Ursi,
1365 A. M.; Temussi, P. A.; Picone, D. Solution Structure of the Alzheimer
Amyloid β -peptide (1-42) in an Apolar Microenvironment. *Eur. J.* **1366**
Biochem. **2002**, *269*, 5642–5648. **1367**
- (86) Innocenti, M.; Salviotti, E.; Guidotti, M.; Casini, A.; Bellandi,
1368 S.; Foresti, M. L.; Gabbiani, C.; Pozzi, A.; Zatta, P.; Messori, L. Trace
1369 Copper(II) or Zinc(II) Ions Drastically Modify the Aggregation
1370 Behavior of Amyloid- β (1-42): An AFM Study. *J. Alzheimer's Dis.* **1371**
2010, *19*, 1323–1329. **1372**
- (87) Pedersen, J. T.; Østergaard, J.; Rozlosnik, N.; Gammelgaard, B.;
1373 Heegaard, N. H. H. Cu(II) Mediates Kinetically Distinct, Non-
1374 amyloidogenic Aggregation of Amyloid- β Peptide. *J. Biol. Chem.* **2011**,
1375 *286*, 26952–26963. **1376**
- (88) Hane, F.; Tran, G.; Attwood, S. J.; Leonenko, Z. Cu²⁺ Affects
1377 Amyloid- β (1-42) Aggregation by Increasing Peptide-peptide Binding
1378 Forces. *PLoS One* **2013**, *8*, No. e59005. **1379**
- (89) Accardo, A.; Shalabaeva, V.; Cotte, M.; Burghammer, M.;
1380 Krahne, R.; Riekel, C.; Dante, S. Amyloid β Peptide Conformational
1381 Changes in the Presence of a Lipid Membrane System. *Langmuir* **1382**
2014, *30*, 3191–3198. **1383**
- (90) Kandel, N.; Zheng, T.; Huo, Q.; Tatulian, S. A. Membrane
1384 Binding and Pore Formation by a Cytotoxic Fragment of Amyloid β
1385 Peptide. *J. Phys. Chem. B* **2017**, *121*, 10293–10305. **1386**
- (91) Liao, Q.; Kamerlin, S. C. L.; Strodel, B. Development and
1387 Application of a Nonbonded Cu²⁺ Model That Includes the Jahn-
1388 Teller Effect. *J. Phys. Chem. Lett.* **2015**, *6*, 2657–2662. **1389**